Biophysical Journal Volume 107 October 2014 1950–1961

Article

Negatively Charged Lipid Membranes Promote a Disorder-Order Transition in the Yersinia YscU Protein

Christoph F. Weise,[1] Frédéric H. Login,[2] Oanh Ho,[1] Gerhard Gröbner,[1] Hans Wolf-Watz,[2] and Magnus Wolf-Watz[1,*]

[1]Department of Chemistry, Chemical Biological Center, Umeå University, Umeå, Sweden; and [2]Department of Molecular Biology and The Laboratory for Molecular Infection Medicine Sweden (MIMS), Umeå Centre for Microbial Research (UCMR), Umeå University, Umeå, Sweden

ABSTRACT The inner membrane of Gram-negative bacteria is negatively charged, rendering positively charged cytoplasmic proteins in close proximity likely candidates for protein-membrane interactions. YscU is a *Yersinia pseudotuberculosis* type III secretion system protein crucial for bacterial pathogenesis. The protein contains a highly conserved positively charged linker sequence that separates membrane-spanning and cytoplasmic ($YscU_C$) domains. Although disordered in solution, inspection of the primary sequence of the linker reveals that positively charged residues are separated with a typical helical periodicity. Here, we demonstrate that the linker sequence of YscU undergoes a largely electrostatically driven coil-to-helix transition upon binding to negatively charged membrane interfaces. Using membrane-mimicking sodium dodecyl sulfate micelles, an NMR derived structural model reveals the induction of three helical segments in the linker. The overall linker placement in sodium dodecyl sulfate micelles was identified by NMR experiments including paramagnetic relaxation enhancements. Partitioning of individual residues agrees with their hydrophobicity and supports an interfacial positioning of the helices. Replacement of positively charged linker residues with alanine resulted in $YscU_C$ variants displaying attenuated membrane-binding affinities, suggesting that the membrane interaction depends on positive charges within the linker. In vivo experiments with bacteria expressing these YscU replacements resulted in phenotypes displaying significantly reduced effector protein secretion levels. Taken together, our data identify a previously unknown membrane-interacting surface of $YscU_C$ that, when perturbed by mutations, disrupts the function of the pathogenic machinery in *Yersinia*.

INTRODUCTION

Disorder-to-order transitions in proteins are encountered in a variety of biochemical contexts (1), such as signal transduction (2) and transcriptional regulation (3). In general, order-to-disorder transitions in proteins occur upon interaction with a template such as another protein or a membrane surface. As an example, the KIX domain of the coactivator CBP folds when bound to a phosphorylated domain of the coactivator CREB (4). Some polypeptides, such as antimicrobial peptides (5) and the Aβ peptide (6), or proteins that are intrinsically disordered in solution, including α-synuclein (7,8), adopt folded structures in the presence of lipid membranes. It has been proposed that in *Escherichia coli* pyruvate oxidase, an order/disorder transition within the context of a membrane binding/folding interaction is a key activation step that exposes the enzymatic binding site to pyruvate in response to reduction of enzyme-bound flavin (9). There exist two extreme models for coupled folding and binding reactions: the induced-fit (10) and conformational-selection (or one-site MWC) (11,12) models. However, recent theoretical and experimental results suggest that in practice, a complex mixture of the two models is used in these reactions (13).

Several Gram-negative bacteria use the type III secretion system (T3SS) to translocate virulence effector proteins into eukaryotic host cells (14). Upon translocation, these effector proteins counteract several immune-defense mechanisms deployed by the host, such as phagocytosis or inflammatory response (15). In *Yersinia*, the effector proteins are denoted *Yersinia* outer proteins (Yops) (16). The T3SS itself is a multiprotein machinery that includes a needle complex that spans both the inner and the outer membranes and ends with a hollow assembly through which effector proteins are believed to be threaded in a nonnative conformation (17). The protein YscU from *Yersinia* and its homologs in other T3SSs are important for the secretion switch from early to late substrates (18–20). YscU contains two domains, an N-terminal membrane-spanning domain (NTD) and a soluble cytoplasmic domain ($YscU_C$) (Fig. 1 *A*). Residues from Ile^{211} through Arg^{239} of $YscU_C$ constitute an evolutionarily conserved linker sequence that separates the folded part of $YscU_C$ from the NTD (Fig. 1, *A* and *B*). During the secretion process, $YscU_C$ undergoes an autoproteolytic cleavage at a conserved NPTH motif. This cleavage generates a cytoplasmic C-terminal peptide ($YscU_{CC}$) of ~10 kDa and a cytoplasmic N-terminal part of $YscU_C$

Submitted June 16, 2014, and accepted for publication September 9, 2014.

*Correspondence: magnus.wolf-watz@chem.umu.se

Christoph F. Weise and Frédéric H. Login contributed equally to this work.

Editor: H. Jane Dyson.

0006-3495/14/10/1950/12 $2.00

http://dx.doi.org/10.1016/j.bpj.2014.09.005

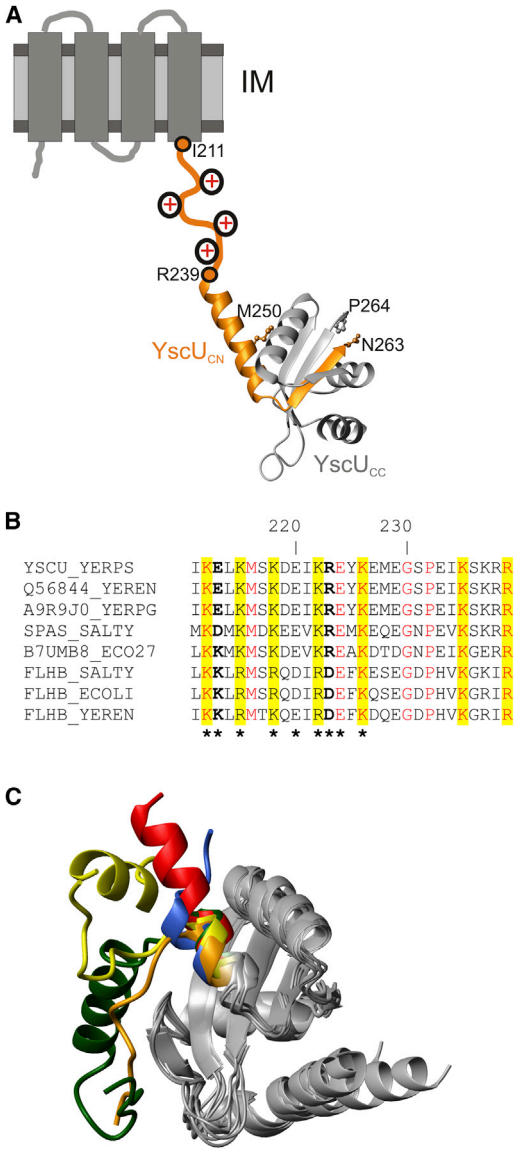

FIGURE 1 YscU$_C$ structure and domain arrangements. (*A*) Representation of the current structural biology view of YscU (25). The membrane-spanning domain (NTD) is illustrated on an IM as four cylinders, and the evolutionarily conserved linker sequence spanning residues Ile^{211} and Gln^{239} is illustrated as an orange line with conserved positive charges added schematically. YscU$_C$ is represented by the crystallographic structure (Protein Data Bank (PDB) code 2JLI (23)). The polypeptides resulting from autoproteolytic cleavage at the (N↑PTH) motif are indicated in orange (YscU$_{CN}$) and gray (YscU$_{CC}$). The C-terminal residue in YscU$_{CN}$ (Asn^{263}) and the N-terminal residue in YscU$_{CC}$ (Pro^{264}) are indicated. Met^{250}, the first structured residue of YscU$_C$ in solution is highlighted. (*B*) The YscU linker sequence contains conserved positively charged side chains. Multiple sequence alignment of YscU (*Y. pseudotuberculosis*), SpaS (*Salmonella typhimurium*), EscU (*Escherichia coli*), and FlhB families from different organisms. Conserved residues that are positively charged are highlighted in yellow. In YscU and SpaS sequences, residues at positions 213 and 223 (*bold*) are negatively or positively charged, whereas they are oppositely charged in the different FlhB proteins. Asterisks indicate residues that were mutated in this study. (*C*) Structural plasticity of the N-terminus in YscU$_C$ and orthologs. Crystallographic structures are superimposed on the core of the autoproteolytic domains using the DALI server (26). The proteins can be identified by the colors of their N-terminal segments: red, *Y. pestis* YscU$_C$ (PDB 2JLI (23)); green, *Y. enterocolitica* YscU$_C^{N263A}$ (PDB 2V5G (25)); yellow, *E. coli* EscU$_C$ (PDB 3BZL (22)); orange, *E. coli* EscU$_C^{T264A}$ (PDB 3BZV (22)); and blue, *S. typhimurium* SpaS$_C$ (PDB 3C01 (22)).

(YscU$_{CN}$) that remains linked to the transmembrane domain (Fig. 1 *A*) (21,22).

YscU$_{CC}$ and YscU$_{CN}$ form a stable complex in solution and the crystallographic structure of this heterodimeric protein has been determined (Fig. 1 (23)). Recently, it was shown that in *Yersinia*, YscU$_{CC}$ dissociates from the remaining membrane-anchored part of YscU (i.e., NTD and YscU$_{CN}$) and is subsequently secreted (24). The crystallographic structure of YscU$_C$ (23) contains an N-terminal α-helix (residues 240–255) that protrudes from the folded core of the protein. In solution, the first 10 amino acid residues in this helix are unstructured and flexible (i.e., the first folded residue is methionine 250), as shown by NMR spectroscopy (24) (Fig. 1 *A*). A comparison between YscU$_C$ homolog structures reveals that whereas the cores of the proteins have very similar structural topology, the N-terminal segments appear to be flexible, adopting helical and/or extended conformations (Fig. 1 *C* (25,26)). Taken together, it appears that the YscU family of linker sequences is disordered in solution but possesses helical propensity that enables crystallization of helical conformations.

Inspection of aligned linker sequences reveals a cluster of conserved positive charges that are distributed with a pattern reminiscent of amphipathic helical periodicity (that is, an i + 3 and i + 4 pattern) (Fig. 1 *B*). Given the boundary conditions that the linker sequence 1), is unstructured in solution; 2), contains stretches of residues with significant helical propensity; 3), has highly conserved positive residues arranged in an amphipathic pattern; and 4), is constrained to be in close proximity to the negatively charged bacterial inner membrane (IM), we designed biophysical experiments to test whether the linker sequence interacts with negatively charged membrane models and whether this interaction is of a disorder-to-order type. We found that the linker sequence indeed interacts with negatively charged membrane models, but it also interacts with vesicles formed from lipid extracts of *E. coli* inner membrane fractions. The interaction occurs in concert with a coil-to-helix transition and as such belongs to the class of proteins that undergo order-to-disorder transitions. An NMR-based structural model of the linker sequence in complex with sodium dodecyl sulfate (SDS) micelles shows the presence of three helical segments. To test the biological significance of the putative linker-IM interaction, we substituted positively charged side chains found on the interaction interface with alanine. These variants displayed attenuated membrane binding affinity in vitro and significantly reduced levels of effector secretion in vivo. In summary, we have identified a disorder-to-order transition in YscU that appears to be significant for *Yersinia* T3SS functionality.

MATERIALS AND METHODS

Bacterial strains, plasmids, and growth conditions

Bacterial strains and plasmids used in this study are listed in Table S2 in the Supporting Material. *E. coli* strains were grown in Luria-Bertani broth (LB) or on Luria agar plates at 37°C. *Yersinia pseudotuberculosis* was grown at either 26°C or 37°C in LB or on Luria agar plates. Antibiotics were used for selection according to the resistance markers carried by the plasmid at concentrations of 50 μg/mL kanamycin and 100 μg/mL carbenicillin. To create calcium-depleted conditions to induce the T3SS, we added 5 mM EGTA and 20 mM $MgCl_2$ into the medium.

Purification of $YscU_{CN}$ variants

yscU$_C$ and *yscU*$_C$[6] were cloned into pGex-6p3 plasmid to produce glutathione-S-transferase (GST)-tagged proteins in BL21 (DE3) pLysS strain. Cultures were first grown at 37°C to $OD_{600} = 0.6$; they were then shifted to 30°C and 1 mM isopropyl β-D-1 thiogalactopyranoside was added to induce protein production for 12 h. Bacteria were harvested by centrifugation at 4600 × *g* and pellets were stored at −80°C. Pellets were resuspended in 50 mM Tris, 2 mM dithiothreitol (DTT), pH 7.4, for sonication and centrifuged at 27,000 × *g* at 4°C. Supernatants were passed through a 0.45 μm syringe filter (Corning, Corning, NY) and loaded on a 5 mL GSTrap FF column (GE Healthcare, Wauwatosa, WI) using an ÄKTA purifier system (GE Healthcare). GST-tagged proteins were eluted with 20 mM glutathione in 50 mM Tris buffer at pH 7.4. Fractions with the fusion protein were pooled, dialyzed against cleavage buffer (50 mM Tris, pH 7.4, 150 mM NaCl, 1 mM EDTA, and 1 mM DTT), and GST was cleaved using PreScission Protease (GE Healthcare) at 4°C overnight. Free GST and remaining GST-tagged protein were eliminated by binding on a GSTrap FF column. $YscU_C$ variants were further purified using cation exchange chromatography (HiTrap SP FF, GE Healthcare). Purified proteins were concentrated using centrifugal filter units (Millipore, Billerica, MA). To dissociate $YscU_{CN}$ from $YscU_{CC}$, $YscU_C$ variants were heated to 70°C and cooled down to 20°C. This treatment triggers $YscU_{CC}$ precipitation, and $YscU_{CN}$ is recovered in the supernatant after centrifugation at 14,000 × *g* at 4°C for 10 min. Slight modifications of the protocol described above were made for the purification of $YscU_{CNK218A}$, $YscU_{CNKE220A}$, and $YscU_{CNR223A}$. Here, *yscU*$_{CN}$ (not *yscU*$_C$) variants were cloned into pGex-6p3. GST-tagged proteins were found mostly in inclusion bodies and were dissolved in 8 M urea, 50 mM Tris, 2 mM DTT, pH 7.4. After centrifugation at 27,000 × *g* to eliminate urea and refold the proteins, the supernatant was stepwise dialyzed against a buffer consisting of 4 M urea, 50 mM Tris, and 2 mM DTT, pH 7.4, for 2 h at 4°C and overnight in the same buffer with no urea. Dialyzed lysates were centrifuged at 27,000 × *g* and 4°C and were loaded onto a 5 mL GSTrap FF column, where the purification was carried out as described above for $YscU_C$ and $YscU_C$[6]. Isotopically enriched proteins ^{15}N and ^{15}N,^{13}C were prepared by growing *E. coli* in an M9 minimal medium supplemented with $^{15}NH_4Cl$ and ^{13}C-D-glucose. Samples containing SDS were prepared by adding an appropriate volume of 200 mM SDS stock solution to $YscU_{CN}$ in buffer.

Preparation of liposomes

1,2-dimyristoyl-*sn*-glycero-3-phosphocholine (DMPC), 1,2-dimyristoyl-*sn*-glycero-3-phospho-(1'-rac-glycerol) (sodium salt) (DMPG), and *E. coli* IM lipid extract were purchased from Avanti Polar Lipids (Alabaster, AL). DMPC or DMPG was dissolved in chloroform or chloroform/methanol (3:1), respectively, to make 2.5 mM stock solutions. Liposomes were prepared by mixing the appropriate volume of stock solutions to get the DMPC/DMPG ratios of 100:0, 95:5, 90:10, 75:25, 50:50, 25:75, and 0:100. The organic solvent was evaporated under a stream of nitrogen gas for 4 h and samples were dried completely under high vacuum overnight. The lipid films were resuspended in 5 mM sodium phosphate, 30 mM NaCl, and 1 mM tris (2-carboxyethyl)phosphine (TCEP), pH 6.0, followed by four freeze-thaw vortexing cycles in liquid nitrogen. Finally, the vesicles were sonicated at 4°C until clear samples were obtained.

Circular dichroism

Far-UV circular dichroism (CD) spectra were recorded on a Jasco J-810 spectropolarimeter (Tokyo, Japan) equipped with a Peltier element for temperature control and a 0.1 cm quartz cuvette. Spectra were recorded from 260 to 195 nm in continuous scanning mode with a response time of 4 s, 0.5 nm steps, a bandwidth of 2 nm, and a scan speed of 50 nm/min. Five spectra were accumulated and averaged to improve the signal/noise ratio. Each spectrum was subtracted with the respective solvent spectrum background. Smoothing of data was performed with a Savitsky-Golay filter with polynomial order 3 and a window frame of 19 points (27). Concentration of added detergents was 2 mM lipid (phospholipid or *E. coli* IM lipid extract) or ~20 mM SDS. For vesicle preparations, 160 μL of 2.5 mM lipid was mixed with 40 μL of 50 μM protein to obtain protein/lipid ratios of 1:200 in each sample. Lipid samples were measured in 5 mM sodium phosphate, 30 mM NaCl, and 1 mM TCEP at pH 7.4. For SDS preparations, 270 μL of 100 μM protein was mixed with 30 μL of 200 mM SDS. SDS samples were measured in 10 mM sodium phosphate at pH 7.4. All samples were homogenized with a vortexer and allowed to equilibrate for at least 15 min before measurement.

NMR spectroscopy

NMR measurements were performed at a $YscU_{CN}$ concentration of 100 μM in 30 mM sodium phosphate and 50 mM NaCl, pH 6.0, with 26 mM SDS and 8% v/v D_2O as a lock solvent. NMR experiments were performed on a Bruker 600 MHz Avance III spectrometer equipped with a 5-mm HCN cryprobe with *z*-axis gradients, using pulse programs from the Bruker library. Temperature calibration was obtained before NMR measurements were taken with a home-built temperature probe inserted into the sample compartment. NMR spectra were processed with NMRPipe (28) and visualized in Ansig for Windows (29) and CcpNmr (30). Resonance assignments of $YscU_{CN}$ in complex with SDS micelles were obtained from ^{15}N NOESY heteronuclear single quantum coherence (HSQC), ^{15}N TOCSY-HSQC (31,32), HNHA (33), HNCA, and HN(CO)CA (34) experiments. Residue-specific secondary structure predictions from pooled $^1H^N$, $^1H^\alpha$, $^{13}C^\alpha$, and ^{15}N chemical shifts were generated with the program MICS (35). Deviations $\Delta\delta = \delta_{obs} - \delta_{rc}$ of observed from random coil shifts were computed using the reference random coil shift database employed by the program MICS (36–38) MICS also provided values of the random coil index (RCI) (39), offering an independent assessment of backbone root mean-square fluctuations to supplement the order parameters derived from spin relaxation measurements. Experimental details regarding structure calculations, amide exchange, pH perturbation, and spin relaxation measurements are outlined in the Supporting Material.

The translational diffusion coefficient of $YscU_{CN}$ in buffer with 26 mM SDS 8% (v/v) D_2O/H_2O was measured at 36.5 ± 0.2°C with a PFG-STE pulse program using binomial pulses for water suppression and a diffusion delay of 100 ms. Amide resonances were integrated and the signal decays fit with a single exponential function by nonlinear least squares to derive the initial signal amplitude, I_0, and diffusion coefficient, D, according to the Stejskal-Tanner equation (40,41):

$$I = I_0 \exp\left[-Dq^2(\Delta - \delta/3)\right]. \quad (1)$$

Here, Δ is the effective diffusion delay and $q = \gamma\delta G$, where γ is the gyromagnetic ratio, and δ and G are the gradient pulse length and amplitude, respectively. Uncertainties in the fitted parameters were estimated from

the root mean-square residuals and the covariance matrix from the fits. The diffusion coefficient of the $YscU_{CN}$ micellar complex was converted into an effective hydrodynamic radius according to the Stokes-Einstein equation (42):

$$D = k_B T/(6\pi\eta r_H). \quad (2)$$

Here, η is the dynamic viscosity of the solvent, r_H is the hydrodynamic radius, k_B is Boltzmann's constant, and T is the absolute temperature. Finally, the hydrodynamic radius was translated into a rotational correlation time using the rotational Stokes-Eintein-Debye equation:

$$\tau_C = V\eta/k_B T, \quad (3)$$

where V is the volume of the tumbling particle, assumed spherical with radius r_H. A value of $\eta = 0.709$ cP for 8% (v/v) D_2O in H_2O at 36.5°C was used in all calculations.

Transverse paramagnetic relaxation enhancements (PREs) were determined by monitoring the effect of doxyl-5-stereate (D5S) and Mn^{2+} on the crosspeak volumes in ^1H-^{15}N HSQC spectra of $YscU_{CN}$. Mn^{2+} PRE spectra were acquired at $MnCl_2$ concentrations of 0, 31, 88, 161, and 225 μM. Measurements with D5S were performed at PRE agent concentrations of 0, 0.43, and 1.93 mM. Crosspeak volumes, V, were fit with Eq. 4 to obtain the transverse PRE rate Γ_2 (43)

$$V[C]/V[0] = \exp[-(R_2 + c\Gamma_2)\tau]/(R_2 + c\Gamma_2), \quad (4)$$

where c is the molar concentration of relaxation agent, τ is the total time during which magnetization is transverse, and R_2 is the effective transverse relaxation rate, estimated as ^{15}N R_2.

Complementation assay

Δ*yscU* (pIB75) strain was transformed with pBAD plasmids encoding either *yscU*wt or different *yscU* point mutants and grown in LB containing both kanamycin and carbenicillin. Cultures in calcium-depleted conditions were started at $OD_{600} = 0.1$, grown at 26°C for 1 h, and shifted to 37°C for 3 h. To analyze Yop secretion, cultures were processed according to the protocol described by Frost and colleagues (24) with some modifications. 9 mL of filtrated supernatant was precipitated with 10% (v/v) of trichloroacetic acid. Cells and supernatants were loaded according to OD_{600} and separated by SDS polyacrylamide gel electrophoresis. Proteins were either stained with Coomassie R250 or, alternatively, transferred onto a polyvinylidene fluoride membrane for immunoblotting. Anti-Yop and anti-YscU antibodies were diluted 1:5000. Horseradish-peroxidase-conjugated anti-rabbit antibody was diluted at 1:10,000 (GE Healthcare). Proteins were detected with a chemiluminescence detection kit (GE Healthcare).

Surface localization of YscF

Surface-localized YscF was analyzed according to the protocol previously described by Edqvist et al. (20), with some modifications. Strains were grown as described above, then gently pelleted and resuspended in LB. The concentrated pellets were sheared by five passages through a hypodermic needle (23G × 1; 0.6 × 25 mm; Braun, Melsungen, Germany) to release surface proteins from the bacterial surface. After centrifugation, sheared supernatants were separated by 15% Tris-Tricine SDS polyacrylamide gel electrophoresis and transferred onto a polyvinylidene fluoride membrane for Immunoblot analysis with anti-YscF antibodies (1:5000 dilution).

RESULTS AND DISCUSSION

Since the IMs of Gram-negative bacteria contain significant amounts of negatively charged lipids (44) and the $YscU_C$ linker sequence is enriched in positively charged residues distributed with an amphipathic helical periodicity, we speculated that the linker can interact with the IM via electrostatic interactions while in a helical conformation. To test this hypothesis we studied the interaction between $YscU_C$ and $YscU_{CN}$ with lipid membrane models of varying complexity. These models that mimic biological membranes range from IM lipid fractions extracted from *E. coli* to glycerophospholipid vesicles composed of varying mixtures of neutral DMPC and negatively charged DMPG lipids to SDS micelles.

$YscU_C$ interacts with negatively charged glycerophospholipid vesicles

To study interactions between $YscU_C$ and membranes, lipid vesicles with a range of negative surface charges were prepared by varying the amount of anionic DMPG lipids incorporated into neutral DMPC bilayers. Far-ultraviolet (far-UV) circular dichroism (CD) spectroscopy is particularly suited to monitor conformational changes in the protein resulting from its association with the membrane (45). As seen in Fig. 2, addition of highly charged DMPG vesicles to $YscU_C$ induces pronounced features in CD bands (208 and 220 nm) that are typical markers for helical secondary structures. These features are much less pronounced in the presence of neutral DMPC vesicles and in the vesicle-free case. This observation is a clear indication that $YscU_C$ indeed can interact with membranes containing anionic lipids, as in the case of the IM, a process that is accompanied by an increase in the helical features of the protein. Since $YscU_C$ does not interact with neutral DMPC vesicles (Fig. 2), the observed interaction is likely caused by electrostatic attraction between basic residues of the protein and the vesicles containing acidic lipid. Fully consistent with a primarily electrostatically driven mechanism, the interaction between $YscU_C$ and DMPG vesicles is screened by addition of potassium chloride (Fig. 2).

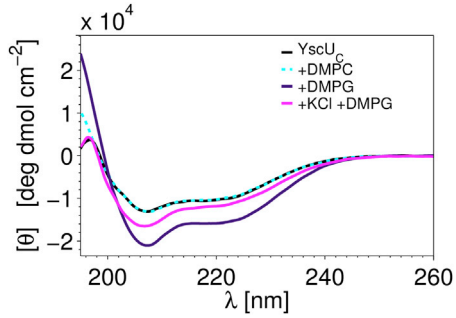

FIGURE 2 $YscU_C$ interacts with negatively charged phospholipid vesicles. The interaction between $YscU_C$ and vesicles was probed with far-UV CD spectroscopy in a buffer consisting of 10 mM sodium phosphate at pH 7.4 and a temperature of 37°C. CD spectra were acquired in buffer (*black*) in the presence of DMPC (zwitterionic; *dashed light blue*) or DMPG vesicles (anionic; *violet*). Addition of 100 mM KCl (*magenta*) attenuated the interaction between $YscU_C$ and DMPG vesicles.

Despite the absence of an increase in helical features upon addition of DMPC, it is possible that the peptide partitions to the membrane interface in a disordered state that would be silent to CD. To check this possibility, we estimated free energies of transfer from water to a neutrally charged membrane environment using the Wimley-White water/interface (w/if) hydrophobicity scale, which describes specifically the free energy of transfer of residues (including peptide bond) within short disordered peptides from water to the interface of POPC large unilamellar vesicles (46). In addition, we calculated traditional hydrophobicities in the form of free energies of transfer from water to octanol (w/o), which is a useful measure of the relative propensity for partitioning to the hydrophobic membrane interior. The large positive values of the w/o and w/if free energies compiled in Table S4 for the entire protein and for individual helices reveal that transfer to a neutral membrane interface or apolar interior is generally disfavored. This is expected for a peptide with such a high proportion of charged residues and supports instead electrostatic attraction as the main driving force for partititioning of the peptide to the vesicle membrane. As a consequence, gain of helical structure can serve as a reporter of binding, and the absence of structure indicates negligible binding to the model membranes used in this study.

Coil-to-helix transition of $YscU_{CN}$

To further characterize the nature of the interactions of $YscU_C$ with negatively charged lipids, we purified $YscU_{CN}$ (residues 211–263; Fig. 1 *A*) and studied its interaction with model membrane systems with different surface potentials and of varying chemical complexity. $YscU_{CN}$ is unstructured in a vesicle-free solution, as indicated by the CD and NMR spectra (Figs. 3 *A* and 4). Like $YscU_C$, $YscU_{CN}$ interacts with anionic lipid vesicles, and this interaction and associated structural changes are strongly correlated with the membrane surface charge density (i.e., the ratio of DMPG to DMPC) as the CD signal varies in a dose-dependent manner with DMPG ratio. The interaction includes an electrostatic component, since it is attenuated in the presence of KCl (Fig. 3 *B*). The CD spectra suggest that $YscU_{CN}$ also undergoes a coil-to-helix transition as a consequence of its association to negatively charged membranes. The nearly complete loss of random-coil character indicated by the CD response reveals that $YscU_{CN}$ is a key site involved in a membrane interaction accompanied by folding of the linker region (Fig. 1 *A*). $YscU_{CN}$ also interacts with SDS micelles and lipid extracts from *E. coli* IM preparations (Fig. 3 *C*). Since *E. coli* and *Yersinia* IM lipids are similar, it is plausible that the protein-membrane interaction also takes place in vivo in *Y. pseudotuberculosis*. The interaction with SDS micelles is important, since it enables a detailed structural characterization of the $YscU_{CN}$-membrane interaction with NMR spectroscopy.

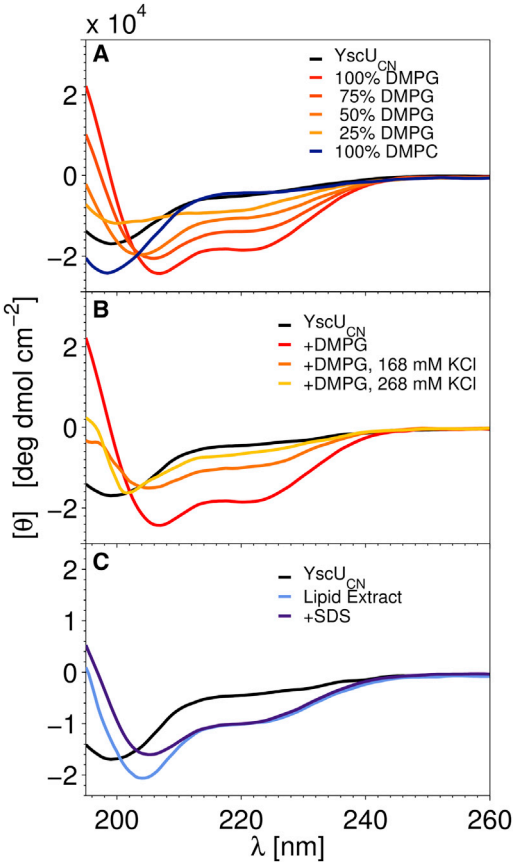

FIGURE 3 $YscU_{CN}$ undergoes a coil-to-helix transition upon binding to negatively charged phospholipid vesicles. The interaction between $YscU_{CN}$ and different membrane models was probed with far-UV CD as in Fig. 2. (*A*) The $YscU_{CN}$ interaction with negatively charged phospholipid vesicles (DMPG) is proportional to negative charge density. (*B*) KCl attenuates the $YscU_{CN}$ interaction with DMPG vesicles in a dose-dependent manner. (*C*) $YscU_{CN}$ interacts with SDS micelles (*purple*) and *E. coli* IM lipid extracts (*light blue*) with a CD response similar to that observed with DMPG vesicles.

$YscU_{CN}$ structure in complex with SDS micelles

To identify the amino acid residues in $YscU_{CN}$ directly involved in the membrane-induced formation of helical segments, we used high-resolution NMR spectroscopy on ^{15}N isotopically enriched $YscU_{CN}$ in complex with negatively charged SDS micelles. Although SDS micelles represent a very basic model of a biological membrane (but contain the characteristic amphiphilic features of a negative surface potential and hydrophobic core), they allow measurement of high-resolution structural information with NMR spectroscopy. The ^{1}H-^{15}N HSQC spectrum of $YscU_{CN}$ in complex with SDS micelles displays well dispersed signals (Fig. 4, *red*) and is significantly shifted from a spectrum obtained in buffer (Fig. 4, *blue*), suggesting that $YscU_{CN}$ forms a stable complex with SDS micelles. An NMR-based determination of the translational diffusion coefficient was used to estimate the size of the protein micelle complex. The diffusion NMR data were satisfactorily fit by a single exponential

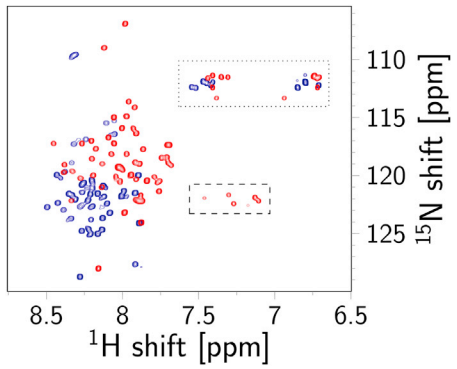

FIGURE 4 Interaction between $YscU_{CN}$ and SDS micelles probed with NMR spectroscopy. ^{1}H-^{15}N HSQC spectra of $YscU_{CN}$ in 30 mM NaPi and 50 mM NaCl, pH 6.0 (*blue*), and in the presence of 26 mM SDS (*red*). The significantly improved signal dispersion of $YscU_C$ when bound to SDS micelles indicates that the protein undergoes a structural rearrangement upon micelle binding. Arginine and glutamine/asparagine side-chain resonances are enclosed in dashed and dotted boxes, respectively.

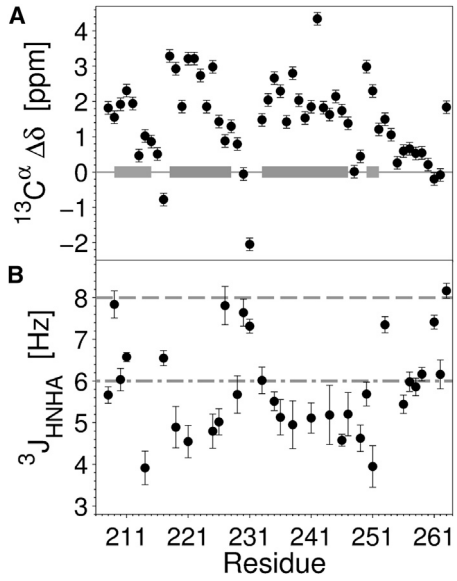

FIGURE 5 NMR identification of helical segments of $YscU_{CN}$ in complex with SDS micelles. (*A*) Deviation ($\Delta\delta$) of observed $^{13}C^{\alpha}$ chemical shifts from random-coil values are displayed against the primary sequence of $YscU_{CN}$. Gray horizontal bars indicate α-helical regions identified by the program MICS (35), with darker tone indicating rigid helices (see Supporting Material). (*B*) $^{3}J_{HNH\alpha}$ couplings in SDS-bound $YscU_{CN}$. Horizontal lines indicate standard cutoffs (48) used during classification of backbone conformations (<6 Hz, α-helical (*dash-dotted gray line*); >8 Hz, extended (*dashed gray line*)).

according to Eq. 1, with uncertainties in D of ±2%. Introduction of a second exponential term did not significantly improve the fits according to an F-statistic. The fitting parameters were insensitive to an increase in the diffusion time from 100 ms to 200 ms. Taken together, the data suggest a reasonable estimate of $1.40 \pm 0.03 \times 10^{-10}$ m^2/s at 36.5°C, which translates to a Stokes hydrodynamic radius of 2.28 ± 0.05 nm. The radius is comparable to previously reported sizes for an SDS micelle (2.34 nm at $c_{SDS} = 26$ mM and $c_{Na^+} = 80$ mM (47)). To derive molecular details on the peptide-micelle interaction, the backbone resonances of $YscU_{CN}$ were assigned in the micelle-bound state using standard NMR approaches (48). Analysis of chemical shifts (35) shows that when interacting with SDS micelles, $YscU_{CN}$ forms three α-helices comprised of more than five residues (Fig. 5 *A*). The existence of these helices is further supported by the magnitudes of three-bond $^{3}J_{HNHA}$ couplings (Fig. 5 *B*) and sequential nuclear Overhauser effect (NOE) patterns (Fig. S1). Thus, the NMR observations reinforce the conclusion from CD spectroscopy that $YscU_{CN}$ undergoes a coil-to-helix transition upon interaction with a negatively charged membrane surface. From NMR structural restraints, an ensemble of conformations (deposited at the Research Collaboratory for Structural Bioinformatics under Protein Data Bank (PDB) code 2ml9) representative of the helical stretches within SDS-bound $YscU_{CN}$ was derived (Fig. 6). Three longer α-helices are evident spanning residues S[0]–K215, K218–E229, and I234–Q246 (residue S[0] is one of the residues encoded by the plasmid multiple cloning site that remain attached to the $YscU_{CN}$ N-terminus after the GST-tag cleavage). Interestingly, the helical segments identified in the presence of SDS agree with secondary structure predictions generated with the PSI-PRED algorithm (49,50) (Fig. S1) and are therefore consistent with similar folded units identified in globular and transmembrane proteins. Molecular structures (Fig. 6) were aligned and rendered with the VMD program (51).

The fast-timescale (picoseconds to nanoseconds) dynamics of the helices was evaluated via NMR-derived order parameters obtained from spin relaxation rates (Fig. S2) and validated independently by chemical-shift measurements via the RCI algorithm (39). The order parameter (S^2) is well suited for quantitative analysis of fast (picoseconds to nanoseconds) internal motions in proteins. It adopts values between 0 and 1, describing the limits of unrestricted versus fully restricted motion on the picosecond-to-nanosecond timescale. Amino acid residues in secondary-structure elements in folded globular proteins usually have order parameters in the range 0.75–0.95 (52). For $YscU_{CN}$ in complex with SDS micelles it was found that helices 2 and 3 have order parameters with a magnitude resembling those of globular proteins, whereas residues in helix 1 have significantly smaller values and consequently are more dynamic on the picosecond-to-nanosecond timescale compared to helices 2 and 3 (Fig. 7). Since helix 1 forms one unit on the basis of NOE connectivities and chemical shifts, it is likely that this helix fluctuates between alternate positions relative to the remainder of the protein.

Helix 2 is initiated by a well defined and conserved N-terminal helix-capping (Ncap) box motif verified by

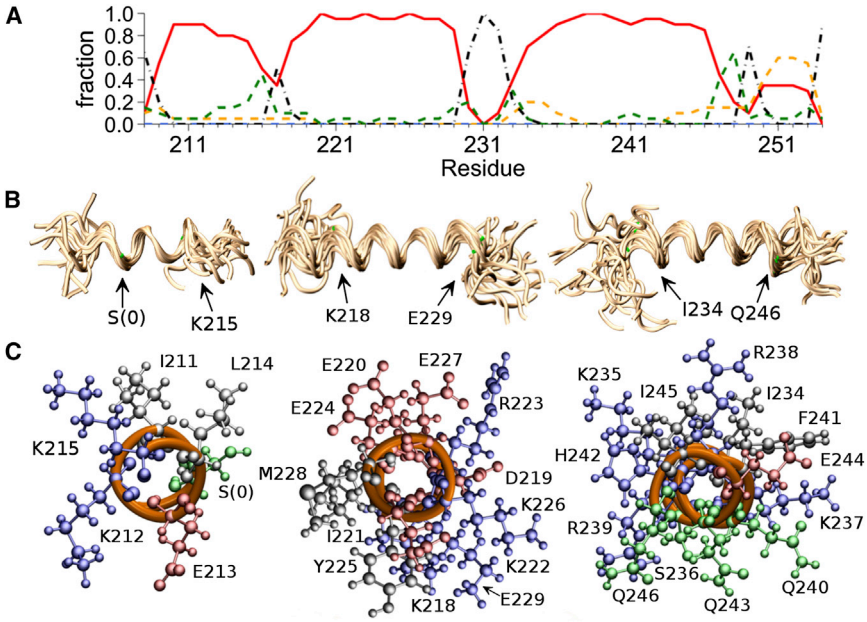

FIGURE 6 Structure of $YscU_{CN}$ in complex with SDS micelles computed from NMR restraints. (*A*) Occupation of different secondary-structure conformations by each residue, averaged over the structure ensemble. Red, α-helix; dashed yellow, 3_{10} helix; dashed green, turn; dash-dotted black, bend or coil. (*B*) Backbone alignments for helices 1–3, showing an ensemble of 20 low-energy conformers. Backbones are rendered as golden coils. Positions of C^{α} atoms at the edges of the aligned segments corresponding to the helix boundaries are marked with green dots and labeled with arrows. (*C*) View along the long axis (from C to N terminus) of the first three helices of $YscU_{CN}$, emphasizing amphipathic helical residue distributions. Backbone atoms are rendered as orange coils and side chains in ball-and-stick format colored according to residue polarity and charge: blue, basic (H, K, and R); red, acidic (D and E); green, polar (S and Q); black, = nonpolar (I, F, M, and Y). Molecular structures were aligned and rendered with the VMD program (51).

the knowledge-based primary sequence and chemical-shift analysis performed with the program MICS. The Ncap is formed by Ser^{217}, which can form a hydrogen bond via its side chain to the backbone amide of Glu^{220}, and a weak NOE is observed between Ser H^{β} and Glu H^{N}, suggesting transient bonding. Helix 3 also displays clear amphipathic periodicity. Although MICS failed to identify probable capping boxes or other bounding motifs in this region, the experimental data are consistent with initiation of the helix at I234 and termination near Q246 (see Fig. 6 *A*). Helices 2 and 3 are separated by the sequence Gly-Ser-Pro-Glu, which is consistent with a type $VI_{\alpha 2/\beta}$ β-turn ($\beta\alpha_R$ or $\beta\beta$ in Ramachandran notation). The key glycine and proline residues in the series are highly conserved (nearly 100%) among $YscU_C$ homologs, and the turn may therefore be of importance for T3SS function.

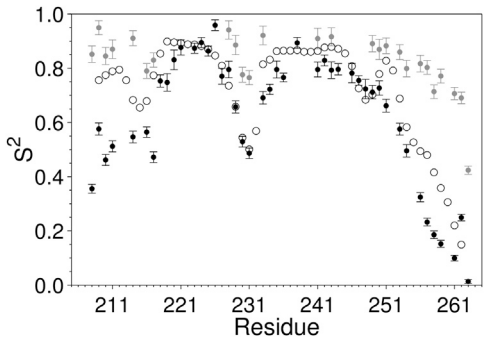

FIGURE 7 Dynamics of $YscU_{CN}$ in complex with SDS. Amplitude of fast-timescale motion (picoseconds to nanoseconds) was quantified by order parameters derived from NMR spin relaxation (S^2 and S^2_{fast}, evaluated at $\tau_M = 7.7$ ns) and chemical shifts (S^2_{RCI}). Solid circles, S^2; gray circles, S^2_{fast}; open circles, S^2_{RCI}.

Positioning of $YscU_{CN}$ in SDS micelles

The positioning of $YscU_{CN}$ within the micellar complex was probed by quantifying the effects of paramagnetic substances added to the bulk solution (Mn^{2+}) or incorporated into the micelle itself in the form of a spin label containing fatty acids (53). Close proximity of a nucleus to the paramagnetic agent enhances NMR spin relaxation, resulting in quantifiable line broadening of NMR resonances. Addition of Mn^{2+} ions to the bulk solution resulted in PREs that are most pronounced for residues in helix 2 and less so for those in helices 1 and 3 (Fig. 8 *A*). These results suggest that helix 2 is located near the surface of the micelle, whereas helices 1 and 3 are more deeply immersed in the hydrophobic core of the micelle. In addition, PREs in helix 2 are most prominent for the acidic glutamic and aspartic acid residues (Fig. 8 *A*, *red*) and weakest for the basic arginine and lysine residues (in blue), which matches the amphipathic pattern of residues in the helices (see Fig. 6 *A*) and is consistent with an interaction primarily driven by positive charges in $YscU_{CN}$. To probe the micellar localization in more detail, additional experiments using micelles doped with D5S were performed. Regions of $YscU_C$ buried within the micelle will be situated closer to the spin-label segment of D5S and thus experience a stronger PRE (see Fig. 8 *B*). Corresponding NMR measurements confirm the buried location of helices 1 and 3 as they display an enhanced PRE. An independent probe of the positioning of $YscU_{CN}$ within the SDS-micellar complex was provided by chemical-shift changes in response to a perturbation of the aqueous buffer surrounding the micelles from pH 6 to 7. In particular $^{1}H^{N}$ and ^{15}N chemical shifts of residues localized in the vicinity of sulfate headgroups at the micellar interface display an amplified sensitivity to buffer pH changes compared to resonances removed from the interface

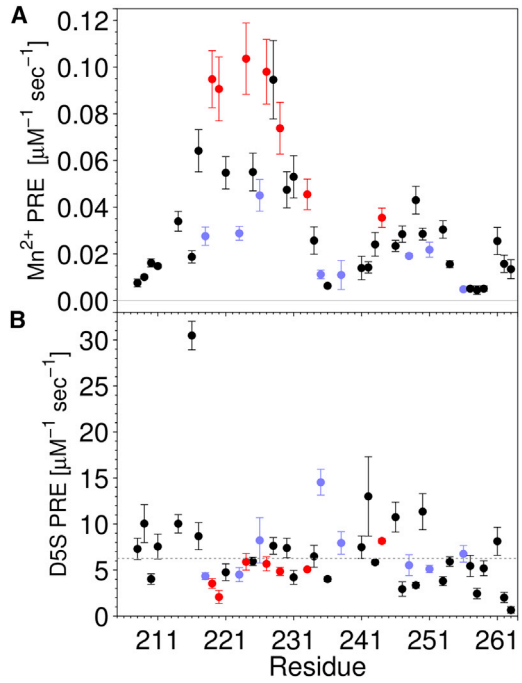

FIGURE 8 Relative solvent exposure of $YscU_{CN}$ residues in the presence of SDS micelles. Paramagnetic relaxation enhancements from titration of SDS-$YscU_{CN}$ complexes with Mn^{2+} (*A*) or D5S (*B*). Red, acidic residues (E and D); blue, basic residues (K and R).

(54) (Figs. S1 and S3). The pH response also places helix 2 at an interfacial location and the other helices at positions more distant from the interface. Amide hydrogen-to-deuterium exchange rates also inform on the position of $YscU_{CN}$ segments within the complex, as their magnitude depends on the extent of solvent exposure. A helix on the surface of a micelle is expected to show less protection against exchange compared to a helix embedded in the micellar core. Quantification of these exchange rates by the CLEANEX approach (55) show that residues in helices 1 and 3 are most protected (Figs. S1 and S4), again substantiating that helix 2 is located at the micelle surface, whereas helices 1 and 3 are less accessible to the solvent. The results of the positioning experiments are consistent with Wimley-White hydrophobicities and Eisenberg hydrophobic moments computed for helices 1–3 (Table S4). The hydrophobicities suggest that compared to helices 1 and 3, helix 2 has a reduced preference for the hydrophobic environment of a micelle or membrane, and the hydrophobic moments indicate that helix 2 would favor an interfacial location relative to the other helices.

It should be noted that differences in the dimensions and chemical composition of an SDS micelle and a phospholipid membrane could alter preferences in location. In particular, constraints imposed upon the dimensions of the SDS complex by the solvation preferences of the amphiphile can be expected to compete with the interactions between helices and to affect the relative positioning of the helices. However, the NMR positioning experiments performed in SDS are useful in providing evidence for interfacial localization of the helices and describing the relative exposure of the individual residues.

Disruption of the $YscU_C$-membrane interaction affects Yop secretion in vivo

The biophysical experiments suggest that the $YscU_C$-membrane interaction is mainly driven by electrostatic attractions, since either incorporation of zwitterionic lipid or addition of salt interfere with $YscU_C$ binding to vesicles. In addition, NMR experiments place helix 2 of $YscU_{CN}$ at the membrane surface. To test whether the proposed membrane interaction in $YscU_C$ is of biological relevance, we performed an alanine scanning mutagenesis toward the positively charged residues within helix 2 and measured the ability of these variants to complement Yop secretion. In a complementation assay, the introduction of a plasmid-encoded copy of *yscU* into a Δ*yscU* strain (i.e., a strain lacking *yscU* gene) restores Yop secretion once the T3SS is activated. The T3SS can be activated by shifting growing bacteria from 26°C to 37°C with a simultaneous depletion of Ca^{2+} from the culture medium by addition of 5 mM EGTA. Hence, depletion of Ca^{2+} and temperature increase are invaluable tools used in the laboratory to mimic the bacterial host cell contact needed for T3SS activation (16). Complementation of Yop secretion was then assayed by introducing plasmids expressing full-length mutated *yscU* in a Δ*yscU* strain. At first, we used the variant denoted $YscU^6$ that contains six alanine substitutions (K212A, K215A, K218A, K222A, R223A, and K226A) to test a variant where the membrane interaction is expected to be removed. Both the empty plasmid and the plasmid-encoding wild-type *yscU* were used as controls to demonstrate the validity of the complementation assay. No complementation of Yop secretion was observed with $YscU^6$ (Fig. 9 *A*), even though the immunoblot showed that similar amounts of Yops were present in the cell pellets (Fig. 9 *B*). Thus, the positively charged residues within helices 1 and 2 are essential for YscU function, and the absence of complementation by $YscU^6$ is probably due to its inability to interact with the IM.

To determine which of those six residues are most important for YscU function, complementation assays were performed with YscU variants containing single substitutions. No significant difference in the level of effector secretion was detected between the wild-type and $YscU_{K212A}$. This result is somewhat surprising considering the degree of conservation of K212 within T3SS homologs (Fig. 1 *B*), and it suggests that this residue is not crucial for YscU function in secretion. A decrease of ~30% and 20% of Yop present in the supernatant was observed for $YscU_{K222A}$ and $YscU_{K226A}$, respectively (Fig. 9). $YscU_{K215A}$, $YscU_{K218A}$, and $YscU_{R223A}$ are the most affected single-substitution variants, with only 50% of secreted Yop compared to the

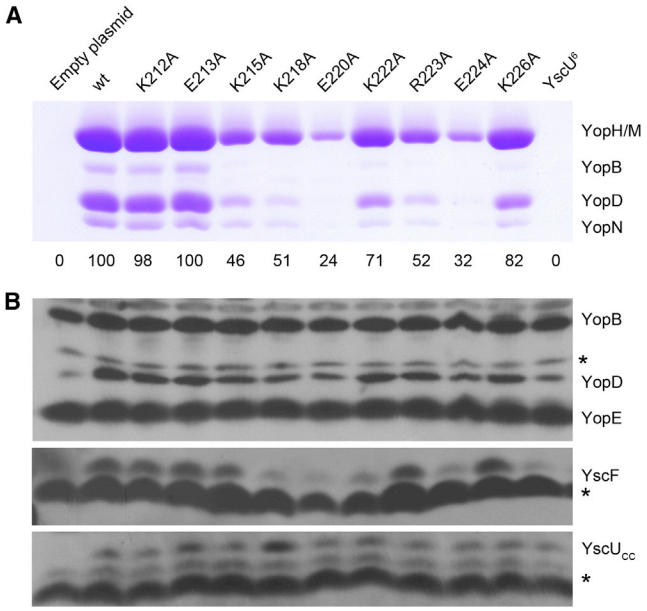

FIGURE 9 Complementation assays to probe the YscU$_C$-membrane interaction in vitro. The Yop secretion complementation assay was performed using a ΔyscU strain. (*A*) Coomassie-stained gel corresponding to trichloroacetic acid precipitated culture supernatants. To compare the complementation efficiency of the different variants, the YopH/M band was quantified by densitometry using MultiGauge software (Fujifilm, Tokyo, Japan). The secretion efficiency has been set to 100 for the strain transformed with the plasmid encoding yscUwt. Quantification results are listed below the gel. (*B*) Cell pellet immunoblots carried out with anti-Yop (*upper*) and anti-YscU$_{CC}$ (*lower*) antibodies and shared supernatants analyzed with an anti-YscF antibody (*center*). Asterisks indicate unspecific bands. To see this figure in color, go online.

wild-type. None of the single mutants abolished Yop secretion as YscU$_C$[6] did, indicating that residues at positions 215, 218, 222, 223, and 226 all participate in the interaction with membranes. It is important to note that synthesis of the effectors is not affected by these substitutions, since a similar amount of Yop was detected in the cell pellets (Fig. 9 *B*). Furthermore, the amount of secreted YscF, the needle subunit that is an early substrate, is also affected. In fact, the amount of secreted effectors is generally proportional to the amount of secreted YscF. These results show that both early substrates and effectors are affected in these mutants.

Mutations of YscU$_{CN}$ at positively charged residues influence the interaction with anionic liposomes

The complementation data presented above suggest that the positively charged residues within YscU$_{CN}$ helices 1 and 2 are critical for YscU function in vitro. To correlate the complementation ability of the different variants with their capacity to interact with negatively charged model membranes we developed a CD-based protocol to measure their interaction with vesicles of varying negative charge density. The-signal at 220 nm (intensity used as a reporter of helical structure) was monitored for the different mutants in a buffer with or without vesicles with different surface charges. For clarity, the mutations in this section are referred to as CN$_X$, where CN corresponds to YscU$_{CN}$ and subscript X defines the mutation position in the peptide sequence. The results displayed in Fig. 10 show that the capacity of CN$_6$ (variant with six substitutions) to interact with the model membrane is significantly reduced compared to the wild-type variant (CN$_{WT}$). This result strongly supports a correlation between the membrane interaction measured in vitro and the in vivo function of the YscU linker within the T3SS. For the two point mutants CN$_{K218A}$ and CN$_{R223A}$, the membrane-interacting capacity is intermediate between the two limiting cases that are CN$_{WT}$ and CN$_6$, which then correlates with partial loss of Yop secretion for these substitutions. Taking all the data together, we observe a correlation between Yop secretion in vivo and membrane-binding capacity in vitro. This observation suggests that the membrane interaction by the linker sequence of YscU is of biological significance. In the model proposed here, the cationic surface of the linker sequence binds to negatively charged membranes in a helical conformation. This raises the possibility that the opposite, solvent-accessible, surface may constitute a binding site for other proteins involved in the secretion process. To test this, we made two point mutations of negatively charged and presumably solvent-exposed side chains (CN$_{E220A}$ and CN$_{E224A}$). Both these substitutions resulted in a significant reduction of effector secretion levels (Fig. 9) while leaving the membrane interaction affinity unaltered compared to that of the wild-type (Fig. 10). These results are consistent with a protein interaction site at the solvent-exposed side of helix 2 that is of functional relevance for effector secretion.

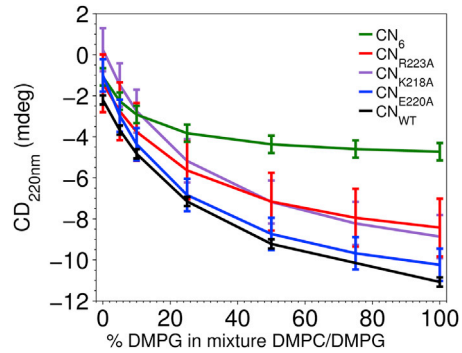

FIGURE 10 Binding of YscU$_{CN}$ and variants to vesicles. The binding capacity of YscU$_{CN}$ variants to vesicles with varying anionic charge density was probed by observing the CD signal at 220 nm. CD spectra were recorded at 20°C in 5 mM sodium phosphate, 30 mM NaCl, and 1 mM TCEP at pH 6.0. The data were analyzed with a one-site binding model (*solid lines*) and the binding capacity is judged from the maximum amplitude of the CD signal. Black, CN$_{WT}$; green, CN$_6$; red, CN$_{R223A}$; purple, CN$_{K218A}$; blue, CN$_{E220A}$.

CONCLUSION

We have found that the linker sequence separating the membrane-spanning and soluble cytoplasmic domains of YscU interacts with negatively charged model membranes. This interaction is dominated by electrostatic contributions, since salt addition attenuates the binding. The interaction is accompanied by extensive acquisition of helical structure. A structural model derived using SDS as a membrane mimic indicates that three helices form in regions that demonstrate clear amphipathic patterns of residue distribution. NMR structural restraints and dynamics measurements indicate that helix 2 has a stable α-helical structure distinctly delineated by strictly conserved features in the amino acid sequence, including helical initiation and termination sites. Together, our observations point to a cooperative (all-or-none) electrostatically mediated binding process. Since the linker sequence is disordered in solution, the membrane induces a disorder-to-order transition. Coupled folding and binding events by unstructured proteins can in principle occur with mixtures of induced fit (10) or conformational selection (11,12) models, but from our equilibrium experiments we cannot distinguish between these models. Disorder-to-order transitions have been observed for other aspects of the T3SS; for instance, YopE undergoes a coupled folding-binding event upon interaction with its chaperone SycE (56). The sequence separating helices 2 and 3 is consistent with a type-VIa/b β-turn and suggests that the helices are primed for an antiparallel alignment, but only when an essential Pro residue in the turn adopts an N-terminal *cis*-amide conformation.

It was found that $YscU_C$ interacts with lipid vesicles from *E. coli* IM extracts, and since the IMs of Gram-negative bacteria are similar, it is likely that some of the interactions we observe with model membranes also occur inside *Yersinia* cells. From a functional standpoint, we have found a correlation between the in vitro membrane-binding capacity of mutated YscUc variants and Yop secretion complementation ability of these mutations when introduced in full-length YscU. From these observations, we propose a model in which the linker sequence of YscU binds to the *Yersinia* IM and suggest that this interaction is important for effector secretion via the T3SS. Supporting our findings, previous works in which mutagenesis toward the linker sequence from *E. coli* EscU (22) and *Salmonella* FlhB (57) showed that small deletions, as well as Proline introduction within the linker sequence, drastically affected T3SS functionality. We propose that membrane interaction would be critical for YscU to be placed in the correct position in relation to the T3SS to fulfill its function. Given the strong linker-sequence conservation between YscU homologs, it is likely that the model proposed here is of relevance also in many other Gram-negative bacterial species.

SUPPORTING MATERIAL

Four tables, four figures, Supporting Experimental Procedures, and Supporting Results and Discussion are available at http://www.biophysj.org/biophysj/supplemental/S0006-3495(14)00941-2.

AUTHOR CONTRIBUTIONS

We thank Konrad Cyprych for assistance with preparation of lipid vesicle samples and Radek Sachl for helpful discussions. Parts of subcloning and protein purification were planned and performed by the Umeå Protein Expertise Platform. The authors declare no conflicts of interest.

This research was financially supported by the Swedish Research Council (M.W.W., H.W.W., and G.G.), an Umeå University Carrier Award to M.W.W., and post-doc support to F.L. from the Umeå Centre for Microbial Research. We acknowledge the Kempe Foundation and the Knut and Alice Wallenberg Foundation for funding of the NMR infrastructure.

SUPPORTING CITATIONS

References (58–79) appear in the Supporting Material.

REFERENCES

1. Radivojac, P., L. M. Iakoucheva, …, A. K. Dunker. 2007. Intrinsic disorder and functional proteomics. *Biophys. J.* 92:1439–1456.
2. Dyson, H. J., and P. E. Wright. 2005. Intrinsically unstructured proteins and their functions. *Nat. Rev. Mol. Cell Biol.* 6:197–208.
3. Uesugi, M., O. Nyanguile, …, G. L. Verdine. 1997. Induced α helix in the VP16 activation domain upon binding to a human TAF. *Science.* 277:1310–1313.
4. Radhakrishnan, I., G. C. Pérez-Alvarado, …, P. E. Wright. 1997. Solution structure of the KIX domain of CBP bound to the transactivation domain of CREB: a model for activator:coactivator interactions. *Cell.* 91:741–752.
5. Shai, Y. 1999. Mechanism of the binding, insertion and destabilization of phospholipid bilayer membranes by α-helical antimicrobial and cell non-selective membrane-lytic peptides. *Biochim. Biophys. Acta.* 1462:55–70.
6. Aisenbrey, C., T. Borowik, …, G. Gröbner. 2008. How is protein aggregation in amyloidogenic diseases modulated by biological membranes? *Eur. Biophys. J.* 37:247–255.
7. Eliezer, D., E. Kutluay, …, G. Browne. 2001. Conformational properties of α-synuclein in its free and lipid-associated states. *J. Mol. Biol.* 307:1061–1073.
8. Varkey, J., J. M. Isas, …, R. Langen. 2010. Membrane curvature induction and tubulation are common features of synucleins and apolipoproteins. *J. Biol. Chem.* 285:32486–32493.
9. Neumann, P., A. Weidner, …, K. Tittmann. 2008. Structural basis for membrane binding and catalytic activation of the peripheral membrane enzyme pyruvate oxidase from *Escherichia coli*. *Proc. Natl. Acad. Sci. USA.* 105:17390–17395.
10. Koshland, D. E. 1958. Application of a theory of enzyme specificity to protein synthesis. *Proc. Natl. Acad. Sci. USA.* 44:98–104.
11. Lange, O. F., N. A. Lakomek, …, B. L. de Groot. 2008. Recognition dynamics up to microseconds revealed from an RDC-derived ubiquitin ensemble in solution. *Science.* 320:1471–1475.
12. Monod, J., J. Wyman, and J. P. Changeux. 1965. On the nature of allosteric transitions: a plausible model. *J. Mol. Biol.* 12:88–118.
13. Dogan, J., S. Gianni, and P. Jemth. 2014. The binding mechanisms of intrinsically disordered proteins. *Phys. Chem. Chem. Phys.* 16:6323–6331.

14. Galán, J. E., and H. Wolf-Watz. 2006. Protein delivery into eukaryotic cells by type III secretion machines. *Nature.* 444:567–573.

15. Mota, L. J., and G. R. Cornelis. 2005. The bacterial injection kit: type III secretion systems. *Ann. Med.* 37:234–249.

16. Cornelis, G. R., and H. Wolf-Watz. 1997. The *Yersinia* Yop virulon: a bacterial system for subverting eukaryotic cells. *Mol. Microbiol.* 23:861–867.

17. Radics, J., L. Königsmaier, and T. C. Marlovits. 2014. Structure of a pathogenic type 3 secretion system in action. *Nat. Struct. Mol. Biol.* 21:82–87.

18. Minamino, T., and R. M. Macnab. 2000. Domain structure of *Salmonella* FlhB, a flagellar export component responsible for substrate specificity switching. *J. Bacteriol.* 182:4906–4914.

19. Williams, A. W., S. Yamaguchi, …, R. M. Macnab. 1996. Mutations in fliK and flhB affecting flagellar hook and filament assembly in *Salmonella typhimurium*. *J. Bacteriol.* 178:2960–2970.

20. Edqvist, P. J., J. Olsson, …, S. A. Lloyd. 2003. YscP and YscU regulate substrate specificity of the *Yersinia* type III secretion system. *J. Bacteriol.* 185:2259–2266.

21. Björnfot, A. C., M. Lavander, …, H. Wolf-Watz. 2009. Autoproteolysis of YscU of *Yersinia pseudotuberculosis* is important for regulation of expression and secretion of Yop proteins. *J. Bacteriol.* 191:4259–4267.

22. Zarivach, R., W. Deng, …, N. C. Strynadka. 2008. Structural analysis of the essential self-cleaving type III secretion proteins EscU and SpaS. *Nature*. 453:124–127.

23. Lountos, G. T., B. P. Austin, …, D. S. Waugh. 2009. Atomic resolution structure of the cytoplasmic domain of *Yersinia pestis* YscU, a regulatory switch involved in type III secretion. *Protein Sci.* 18:467–474.

24. Frost, S., O. Ho, …, M. Wolf-Watz. 2012. Autoproteolysis and intramolecular dissociation of *Yersinia* YscU precedes secretion of its C-terminal polypeptide YscU(CC). *PLoS ONE.* 7:e49349.

25. Wiesand, U., I. Sorg, …, D. W. Heinz. 2009. Structure of the type III secretion recognition protein YscU from *Yersinia enterocolitica*. *J. Mol. Biol.* 385:854–866.

26. Holm, L., and P. Rosenström. 2010. Dali server: conservation mapping in 3D. *Nucleic Acids Res.* 38:W545–W549.

27. Greenfield, N. J. 2006. Using circular dichroism spectra to estimate protein secondary structure. *Nat. Protoc.* 1:2876–2890.

28. Delaglio, F., S. Grzesiek, …, A. Bax. 1995. NMRPipe: a multidimensional spectral processing system based on UNIX pipes. *J. Biomol. NMR.* 6:277–293.

29. Helgstrand, M., P. Kraulis, …, T. Härd. 2000. Ansig for Windows: an interactive computer program for semiautomatic assignment of protein NMR spectra. *J. Biomol. NMR.* 18:329–336.

30. Vranken, W. F., W. Boucher, …, E. D. Laue. 2005. The CCPN data model for NMR spectroscopy: development of a software pipeline. *Proteins.* 59:687–696.

31. Palmer, A. G., J. Cavanagh, …, M. Rance. 1991. Sensitivity improvement in proton-detected two-dimensional heteronuclear correlation NMR spectroscopy. *J. Magn. Reson.* 93:151–170.

32. Kay, L. E., P. Keifer, and T. Saarinen. 1992. Pure absorption gradient enhanced heteronuclear single quantum correlation spectroscopy with improved sensitivity. *J. Am. Chem. Soc.* 114:10663–10665.

33. Vuister, G. W., and A. Bax. 1993. Quantitative J correlation: a new approach for measuring homonuclear 3-bond $J(H^{N}H\alpha)$ coupling constants in ^{15}N-enriched proteins. *J. Am. Chem. Soc.* 115:7772–7777.

34. Grzesiek, S., and A. Bax. 1992. Improved 3D triple-resonance NMR techniques applied to a 31 kDa protein. *J. Magn. Reson.* 96:432–440.

35. Shen, Y., and A. Bax. 2012. Identification of helix capping and b-turn motifs from NMR chemical shifts. *J. Biomol. NMR.* 52:211–232.

36. Cornilescu, G., F. Delaglio, and A. Bax. 1999. Protein backbone angle restraints from searching a database for chemical shift and sequence homology. *J. Biomol. NMR.* 13:289–302.

37. Spera, S., and A. Bax. 1991. Empirical correlation between protein backbone conformation and Cα and Cβ ^{13}C nuclear magnetic resonance chemical shifts. *J. Am. Chem. Soc.* 113:5490–5492.

38. Wishart, D. S., C. G. Bigam, …, B. D. Sykes. 1995. ^{1}H, ^{13}C and ^{15}N random coil NMR chemical shifts of the common amino acids. I. Investigations of nearest-neighbor effects. *J. Biomol. NMR.* 5:67–81.

39. Berjanskii, M. V., and D. S. Wishart. 2007. The RCI server: rapid and accurate calculation of protein flexibility using chemical shifts. *Nucleic Acids Res.* 35:W531–W537.

40. Price, W. S. 1998. Pulsed-field gradient nuclear magnetic resonance as a tool for studying translational diffusion: Part II. Experimental aspects. *Concepts Magn. Reson.* 10:197–237.

41. Stejskal, E. O., and J. E. Tanner. 1965. Spin diffusion measurements: spin echoes in the presence of a time-dependent field gradient. *J. Chem. Phys.* 42:288–292.

42. Price, W. S. 1997. Pulsed-field gradient nuclear magnetic resonance as a tool for studying translational diffusion. 1. Basic theory. *Concepts Magn. Reson.* 9:299–336.

43. Battiste, J. L., and G. Wagner. 2000. Utilization of site-directed spin labeling and high-resolution heteronuclear nuclear magnetic resonance for global fold determination of large proteins with limited nuclear overhauser effect data. *Biochemistry.* 39:5355–5365.

44. Silhavy, T. J., D. Kahne, and S. Walker. 2010. The bacterial cell envelope. *Cold Spring Harb. Perspect. Biol.* 2:a000414.

45. Unnerståle, S., L. Mäler, and R. R. Draheim. 2011. Structural characterization of AS1-membrane interactions from a subset of HAMP domains. *Biochim. Biophys. Acta.* 1808:2403–2412.

46. White, S. H., and W. C. Wimley. 1998. Hydrophobic interactions of peptides with membrane interfaces. *Biochim. Biophys. Acta.* 1376:339–352.

47. Quina, F. H., P. M. Nassar, …, B. L. Bales. 1995. Growth of sodium dodecyl sulfate micelles with detergent concentration. *J. Phys. Chem.* 99:17028–17031.

48. Cavanagh, J., W. J. Fairbrother, …, N. J. Skelton. 1996. Protein NMR Spectroscopy: Principles and Practice. Academic Press, San Diego.

49. Buchan, D. W., S. M. Ward, …, D. T. Jones. 2010. Protein annotation and modelling servers at University College London. *Nucleic Acids Res.* 38:W563–W568.

50. Jones, D. T. 1999. Protein secondary structure prediction based on position-specific scoring matrices. *J. Mol. Biol.* 292:195–202.

51. Humphrey, W., A. Dalke, and K. Schulten. 1996. VMD: visual molecular dynamics. *J. Mol. Graph.* 14:33–38, 27–28.

52. Goodman, J. L., M. D. Pagel, and M. J. Stone. 2000. Relationships between protein structure and dynamics from a database of NMR-derived backbone order parameters. *J. Mol. Biol.* 295:963–978.

53. Jarvet, J., J. Danielsson, …, A. Gräslund. 2007. Positioning of the Alzheimer Aβ(1–40) peptide in SDS micelles using NMR and paramagnetic probes. *J. Biomol. NMR.* 39:63–72.

54. Sheftic, S. R., R. L. Croke, …, A. T. Atexandrescu. 2009. Electrostatic contributions to the stabilities of native proteins and amyloid complexes. *Methods Enzymol.* 466:233–258.

55. Hwang, T. L., P. C. van Zijl, and S. Mori. 1998. Accurate quantitation of water-amide proton exchange rates using the phase-modulated CLEAN chemical EXchange (CLEANEX-PM) approach with a Fast-HSQC (FHSQC) detection scheme. *J. Biomol. NMR.* 11:221–226.

56. Rodgers, L., A. Gamez, …, P. Ghosh. 2008. The type III secretion chaperone SycE promotes a localized disorder-to-order transition in the natively unfolded effector YopE. *J. Biol. Chem.* 283:20857–20863.

57. Fraser, G. M., T. Hirano, …, R. M. Macnab. 2003. Substrate specificity of type III flagellar protein export in *Salmonella* is controlled by subdomain interactions in FlhB. *Mol. Microbiol.* 48:1043–1057.

58. Schwieters, C. D., J. J. Kuszewski, and G. M. Clore. 2006. Using Xplor-NIH for NMR molecular structure determination. *Prog. Nucl. Magn. Reson. Spectrosc*. 48:47–62.

59. Schwieters, C. D., J. J. Kuszewski, …, G. M. Clore. 2003. The XplorNIH NMR molecular structure determination package. *J. Magn. Reson.* 160:65–73.

60. Shen, Y., F. Delaglio, …, A. Bax. 2009. TALOS+: a hybrid method for predicting protein backbone torsion angles from NMR chemical shifts. *J. Biomol. NMR.* 44:213–223.

61. Laskowski, R. A., M. W. Macarthur, …, J. M. Thornton. 1993. Procheck: a program to check the stereochemical quality of protein structures. *J. Appl. Crystallogr.* 26:283–291.

62. Kabsch, W., and C. Sander. 1983. Dictionary of protein secondary structure: pattern recognition of hydrogen-bonded and geometrical features. *Biopolymers.* 22:2577–2637.

63. Eisenberg, D., R. M. Weiss, and T. C. Terwilliger. 1984. The hydrophobic moment detects periodicity in protein hydrophobicity. *Proc. Natl. Acad. Sci. USA.* 81:140–144.

64. Kay, L. E., D. A. Torchia, and A. Bax. 1989. Backbone dynamics of proteins as studied by ^{15}N inverse detected heteronuclear NMR spectroscopy: application to staphylococcal nuclease. *Biochemistry.* 28:8972–8979.

65. Mori, S., C. Abeygunawardana, …, P. C. van Zijl. 1995. Improved sensitivity of HSQC spectra of exchanging protons at short interscan delays using a new fast HSQC (FHSQC) detection scheme that avoids water saturation. *J. Magn. Reson. B.* 108:94–98.

66. Bai, Y., J. S. Milne, …, S. W. Englander. 1993. Primary structure effects on peptide group hydrogen exchange. *Proteins.* 17:75–86.

67. Connelly, G. P., Y. Bai, …, S. W. Englander. 1993. Isotope effects in peptide group hydrogen exchange. *Proteins.* 17:87–92.

68. Markley, J. L., A. Bax, …, K. Wüthrich. 1998. Recommendations for the presentation of NMR structures of proteins and nucleic acids. *J. Mol. Biol.* 280:933–952.

69. Mandel, A. M., M. Akke, and A. G. Palmer, 3rd. 1995. Backbone dynamics of *Escherichia coli* ribonuclease HI: correlations with structure and function in an active enzyme. *J. Mol. Biol.* 246:144–163.

70. Fushman, D., S. Cahill, and D. Cowburn. 1997. The main-chain dynamics of the dynamin pleckstrin homology (PH) domain in solution: analysis of ^{15}N relaxation with monomer/dimer equilibration. *J. Mol. Biol.* 266:173–194.

71. Hall, J. B., and D. Fushman. 2003. Characterization of the overall and local dynamics of a protein with intermediate rotational anisotropy: differentiating between conformational exchange and anisotropic diffusion in the B3 domain of protein G. *J. Biomol. NMR.* 27:261–275.

72. Wennerst, H. 1972. Nuclear magnetic relaxation induced by chemical exchange. *Mol. Phys.* 24:69–80.

73. Lipari, G., and A. Szabo. 1982. Model-free approach to the interpretation of nuclear magnetic-resonance relaxation in macromolecules. 1. Theory and range of validity. *J. Am. Chem. Soc.* 104:4546–4559.

74. Lipari, G., and A. Szabo. 1982. Model-free approach to the interpretation of nuclear magnetic resonance relaxation in macromolecules. 2. Analysis of experimental results. *J. Am. Chem. Soc.* 104:4559–4570.

75. Clore, G. M., A. Szabo, …, A. M. Gronenborn. 1990. Deviations from the simple two-parameter model-free approach to the interpretation of nitrogen-15 nuclear magnetic relaxation of proteins. *J. Am. Chem. Soc.* 112:4989–4991.

76. Ortega, A., and J. G. de la Torre. 2003. Hydrodynamic properties of rodlike and disklike particles in dilute solution. *J. Chem. Phys.* 119:9914–9919.

77. Ma, K., E. L. Clancy, …, M. G. Zagorski. 1999. Residue-specific pK_a measurements of the β-peptide and mechanism of pH-induced amyloid formation. *J. Am. Chem. Soc.* 121:8698–8706.

78. Studier, F. W., and B. A. Moffatt. 1986. Use of bacteriophage T7 RNA polymerase to direct selective high-level expression of cloned genes. *J. Mol. Biol.* 189:113–130.

79. Lavander, M., L. Sundberg, …, A. Forsberg. 2002. Proteolytic cleavage of the FlhB homologue YscU of *Yersinia pseudotuberculosis* is essential for bacterial survival but not for type III secretion. *J. Bacteriol.* 184:4500–4509.

SUPPLEMENTAL INFORMATION

Negatively charged lipid membranes promote a disorder-order transition in the Yersinia YscU Protein

Christoph F. Weise[‡1], Frédéric H. Login[§], Oanh Ho[‡], Gerhard Gröbner[‡], Hans Wolf-Watz[§] and Magnus Wolf-Watz[‡2]

[‡]Department of Chemistry, Chemical Biological Center, Umeå University, SE- 901 87 Umeå, Sweden

[§] Department of Molecular Biology and The Laboratory for Molecular Infection Medicine Sweden (MIMS), Umeå Centre for Microbial Research (UCMR), Umeå University, SE-901 87 Umeå, Sweden

SUPPLEMENTAL EXPERIMENTAL PROCEDURES

Structure calculation from NMR restraints with XPLOR-NIH

NOEs, chemical shifts and $^{3}J_{HNHA}$ couplings were combined as restraints during generation of a conformational ensemble by implementing simulated annealing and molecular dynamics with the XPLOR-NIH package (vs. 2.33) (1, 2). Supplementary Table S1 summarizes the number of NMR restraints (300 total) collected, according to type. NOE restraint tables were generated with the program Ansig for windows (3) from a 3D NOESY spectrum. Crosspeak volumes were normalized to the mean value and classified as weak if I<0.87, intermediate if 0.87<I<5 and strong if I>5. A quadratic distance restraint potential was implemented with a lower bound of 1.8 Å and the following upper bounds: weak, r_{upper} = 6.0 Å; intermediate, r_{upper} = 3.6 Å; strong, r_{upper} = 2.7 Å. Chemical shifts ($^{1}H^{\alpha}$, $^{1}H^{N}$, $^{13}C^{\alpha}$ and ^{15}N) were converted into dihedral restraints using TALOS+ (4). Dihedral angles classified as ambiguous or highly dynamic by TALOS+ were excluded. $^{3}J_{HNHA}$ coupling restraints were implemented with a J-coupling potential using the following Karplus parameters: A=6.98, B=-1.38, and C=1.72, and a minimum uncertainty in ^{3}J of 0.5 Hz. Database or covalent restraints were implemented for bond lengths, angles, dihedrals, van der Waals contacts and hydrogen bonds. A mean-field database-derived Ramachandran torsion angle potential was employed to maintain backbone dihedral angles within favored regions for residues lacking sufficient restraints, particularly at the termini and interhelical regions (residues <212, >252, 229-233). Initial conformations were generated by imposing backbone dihedral angles corresponding to the TALOS+ restraints on a randomized conformation. The initial simulated annealing protocol consisted of high temperature dynamics for 800 ps at 3500 K followed by slow

cooling to 25 K in 12.5 K, 0.2 ps steps while switching on the NMR restraints. This was followed by energy minimizations in torsion-angle and then Cartesian space. The annealing/minimization cycles were iterated to generate 100 initial structures. Of these, the 20 lowest in energy satisfying the NMR restraints and PROCHECK criteria were selected (5). The preference of each residue for different secondary structure conformations was computed with program DSSP (6). by averaging over the ensemble of NMR structures. The limits of individual helices were defined for use in computation of charges, hydrophobicities (7)) and hydrophobic moments (8) from the DSSP averages using a value of 0.75 as the minimum helical population defining a residue as part of a helix.

NMR spin relaxation

Backbone amide ^{15}N R_1, R_2 and ^{15}N-^{1}H NOE measurements were performed with phase-sensitive gradient-enhanced ^{15}N-^{1}H PEP-HSQC pulse programs with flip-back pulses and GARP decoupling during acquisition (9). R_1 data was acquired with DIPSI2 ^{1}H decoupling during relaxation delays of 0.100, 0.150, 0.250, 0.370, 0.510 0.825, 1.05, and 1.50 s. For R_2 experiments relaxation delays of 17, 52, 86, 138, 173, 242, 294 and 346 ms were used. ^{15}N-^{1}H NOE spectra were acquired in an interleaved manner, with a 5 s relaxation delay and a 3 s NOE buildup period. Relaxation rates R_1 and R_2 were derived from non-linear least-squares fits (Levenberg-Marquardt algorithm) with single exponential functions, $I[t] = I[0] \exp(-t R_{1/2})$, with t the relaxation delay and I[t] the crosspeak volume. Uncertainties in the $R_{1,2}$ relaxation parameters were derived from the parameter covariance matrix combined with uncertainties in integrated crosspeak

volumes estimated from the baseline RMS noise level. Uncertainties in the NOEs were derived from the RMS baseline noise and crosspeak volumes. Complete relaxation data was obtained for 41 of 52 $YscU_{CN}$ residues unaffected by resonance overlap as well as 3 residues from the construct linker (Fig. S2). For NMR relaxation measurements and other HSQC-based experiments, resonance overlap interfered with quantification for the following residues at pH 6.0: K212, E213, K215, K222, K237, R239, Q240, I245, E252, K255, and V260.

pH Perturbation

As an additional probe of solvent exposure, the effect of a pH perturbation on chemical shifts was monitored by acquiring ^{1}H-^{15}N HSQC spectra at pH 6.0 and 7.0. Water was employed as an internal reference using the known dependence of its chemical shift on pH and temperature. The chemical shift response $\Delta\delta$ of backbone amide $^{1}H^{N}$ and ^{15}N with the pH change were used to compute a mean response according to Equation S1:

$$\delta_{avg} = [\Delta\delta_H^2 + (0.15\Delta\delta_N)^2]^{1/2} \qquad \textbf{(Equation S1)}$$

Amide Exchange Measurements

Exchange of protein amide protons (H^N) with water was monitored by NMR to discriminate shielded from solvent accessible regions of the backbone amide groups. The CLEANEX-PM-FHSQC experiment was employed to measure the exchange rate k_{ex} under fast exchange conditions ($k_{ex}>1\ s^{-1}$) (10). CLEANEX-PM mixing delays of 100 ms and 300 ms were applied. Crosspeak volumes in the exchange spectra were normalized

to integrals from a reference FHSQC spectrum (11). Residues I221, E233, M250 and V259 with strongly overlapping HSQC crosspeaks were excluded from the analysis.

The exchange buildup curves were fit with Equation 1 from Ref. ((10)) to derive k_{ex}. The buildup process is determined by k_{ex} and by the relaxation rates of amide and solvent magnetizations. The effective relaxation rate of water, a uniformly valued (global) parameter in all of the fits, was fixed at a value of 0.6 s^{-1} based on an independent measurement (10). Lower and upper bounds for the relaxation rate R_{1A} of 0.01 s^{-1} and 50 s^{-1} were selected based on $^1H^N$ R_1 and R_2 rates estimated from the global correlation time of the micellar aggregate and a dipolar interaction with a minimum interproton distance of 2 Å. Solvent protection factors $P_{solv}=k_{rc}/k_{prot}$ were computed from reference random coil exchange rates k_{rc} obtained with the program SPHERE (http://www.fccc.edu/research/labs/roder/sphere) using the standard parameter set for poly-DL-alanine (12) (13) and activation energies derived from the high-temperature behavior of BPTI and Ribonuclease A. Large uncertainties ($\sigma_s \approx k_{ex}$) in fitted parameters and computed protection factors were obtained for residues I211, L214, R223, K226, E244, and I245. For these residues the large uncertainty is due to a small signal buildup attributed to a small k_{ex} (<0.4 s^{-1}) and associated large protection factor ($k_{rc} >> k_{ex}$).

SUPPLEMENTAL RESULTS AND DISCUSSION

Structure Prediction from NOEs, Chemical Shifts, and $^3J_{HNHA}$ Couplings

The $^3J_{HNHA}$ spin-spin coupling constant is diagnostic of the value of the backbone dihedral angle ϕ: $^3J_{HNHA}$ <6 Hz is indicative of α-helical structure while $^3J_{HNHA}$>8 Hz is consistent with extended conformations (14). Couplings were obtained for 34 of 55 backbone residues in SDS-complexed $YscU_{CN}$ (Fig. 5B). Most values for residues in the range D219-S258 are consistent with α-helical conformation. Exceptions occur at residues S217, E227, G230-S231 and N253, which display intermediate coupling magnitudes suggestive of large-amplitude conformational sampling. Couplings for residues above S257 and below residue I211 also lie near or above 6 Hz, pointing to the predominance of disordered conformations at the termini, and only residue N263 has a coupling strongly suggestive of an extended conformation.

Helical regions predicted from the input primary amino acid sequence and $^1H^{\alpha}$, $^1H^{N}$, $^{13}C^{\alpha}$ and ^{15}N chemical shifts by program MICS are overlayed in Fig. 5A onto deviations $\Delta\delta$ of $^{13}C^{\alpha}$ shifts from random coil values. The ordered regions predicted by MICS are almost exclusively helical. MICS identified three helical stretches of 5 or more residues and three 2-3 residue spans exhibiting helical character. The longer helical stretches G[-1]-K215, K218-M228, and E233-S247 coincide with regions exhibiting $^3J_{HNHA}$ and ^1H-^1H dipole coupling patterns characteristic of α-helical conformation. Negative $\Delta\delta$ $^{13}C^{\alpha}$ for S217 and particularly the large negative value (-2.0 Hz) for S231 point to an extended conformation. MICS suggested a cap structure for residue S217 as part of a helical N-capping motif (Q=0.89). Other notable structural motifs suggested by the primary sequence include a type-VI β-turn involving residues G230-E233 (MICS is not trained

for identification of this type of β-turn). The remaining residues are predicted to be within loops.

The helical stretches identified on the basis of NOEs, chemical shifts, and $^{3}J_{HNHA}$ agree well with the predictions of program PSI-PRED based on the primary sequence of $YscU_{CN}$ (15) (16) (Fig. S1). Both MICS and PSI-PRED make predictions based on prior knowledge in the form of experimental structure and/or chemical shift databases. The agreement between the helical regions identified in a membrane-mimicking environment and predictions based on a database of reported protein structures can reflect universal principles guiding helix formation. Minor differences do arise between the predictions of MICS versus PSI-PRED. For instance, the third helix predicted by PSI-PRED extends up to N253, further than S247 as suggested by MICS, incorporating the short helical stretch M250-E252 also identified by MICS. There remains some ambiguity with regard to the termination point of helix 3. It is perhaps no coincidence that crystal structures of different $YscU_{C}$ homologues provide mixed predictions on helical structure within the second half of $YscU_{CN}$ (residues > R239, see Fig. 1C).

Structure calculations

Supplementary Table S1 summarizes the validation results for the 20 low energy structures generated by imposing NMR restraints during XPLOR-NIH simulations of $YscU_{CN}$. Deviations between restraints and computed distances, dihedral angles and $^{3}J_{HNHA}$ couplings were generally small with only minor violations. Structure ensemble, restraints list and chemical shifts are available at the BMRB and RCSB data banks (BMRB ID 19809 and PDB ID 2ml9). Although structures with backbone dihedral angles

in Ramachandran regions labeled as unallowed by PROCHECK were excluded, the absence of NMR restraints in loop and terminal regions (<K212, >E252, G230-E233) led to a significant population of generously allowed backbone conformations (uncommonly observed in databases) among those residues. The reported backbone conformation of these loop and terminal residues is not meaningful insofar as they were not subject to NMR restraints but only depend on the intrinsic XPLOR-NIH potential terms. In addition, the ϕ/ψ dihedrals for residues M216-S217 and R248-N249, for which available NMR restraints were applied, were also prone to borderline values, which can be attributed to the labile nature of these regions at the interface with the disorganized loops/termini, and is reflected in the $^{13}C^{\alpha}$ chemical shifts and dihedral angles predicted by TALOS+ for those residues. Residues undergoing larger amplitude conformational exchange would be better described by ensemble simulations.

Residue-specific secondary structure conformational preferences computed with program DSSP and averaged over the ensemble of NMR structures are displayed in Fig. 6A. The three stretches marked by high occupation (population>0.75) of α-helical conformations are clearly identified, spanning residues S[0]-K215, K218-E229, and I234-Q246. A shorter stretch involving M250-N253 exhibits a mixture of α-helical and primarily 3_{10} helical conformation. The helical stretches are in good agreement with the predictions provided by MICS on the basis of chemical shifts. The preservation of α-helical regions over the ensemble is shown in the close registry of backbones following alignment (Fig. 6B). Conformational variation in helix 2 is less than in helices 1 and 3 consistent with the greater number of NOE restraints observed in this region. The edges of helix 3 exhibit some variation (~20%) in the form of 3_{10} helical structures. Helix 1 also

shows heterogeneity including turn-like conformations particularly near helix 2. In addition, in ~33% of the structures the helical conformation extended between residues in helix 1 and 2, i.e. included M216 and S217.

NMR spin relaxation

Parameters describing global and residue-specific motions were derived from pooled ^{15}N R_1 and R_2 and ^{15}N-^{1}H NOE values (Fig. S2) for the 44 residues for which complete relaxation data was available, implementing a "modelfree" protocol similar to that outlined by Mandel *et al.* (17) with the program Dynamics (18-20). In the absence of a known structure for the protein fragment it was not possible to derive a full rotational diffusion tensor from the relaxation dataset alone. The global motion was therefore assumed to be described by an isotropic rotational tensor with a single correlation time τ_M. The assumption of isotropic motion is a reasonable first approximation consistent with the tendency of SDS to form spherical aggregates. The availability of data at only one magnetic field further constrained the choice of motional model to ones with three or less adjustable parameters. Standard models based on the model-free formalism of Lipari and Szabo (21, 22) were evaluated. In order of increasing complexity (number of fitting parameters), these are: LS model with very fast internal motions (τ_i 0, model 1); full LS model (model 2); fast LS model with a chemical exchange (R_{2ex}) contribution to R_2 ((23)); LS model with an R_{2ex} contribution (model 4); Clore's extended LS model with two timescales of internal motion (model 5 (23)). The parameters describing local motions are R_{2ex}, and the order parameter (S^2) and internal correlation time τ_i associated with the N-H bond vector. An appropriate value of the global correlation time was

selected using a grid search. During selection of a local motional model for each residue, local dynamic parameters were optimized *via* non-linear least-squares fits at preset values of the global correlation time on the τ_M grid. For each residue, an optimal model was selected based on two criteria: (1) a value of the goodness-of-fit sum-of-squares statistic χ^2_i within the 90% confidence interval; and (2) F-tests to compare alternative nested models, with rejection of the more complex model if the F-statistic falls within the 80% confidence interval. The performance of fits at different values of τ_M was assessed using the global sum-of-squares χ^2_{tot} and a reduced statistic $\chi^2_{red} = \chi^2_{tot}/n_{DF}$, where n_{DF} is the cumulative number of degrees of freedom. Uncertainties in the local motional parameters were estimated with the Monte Carlo approach implemented within Dynamics by fitting 500 mock data sets generated using the experimental data as template.

Internal and global dynamics from NMR relaxation data

Values of the global rotational correlation time τ_M and of local motional parameters S^2, τ_i, and R_{2ex} for SDS-associated $YscU_{CN}$ were derived from pooled ^{15}N R_1, R_2 and ^{15}N-^1H NOEs. The relaxation data analysis included residues >R251, <K218, and E229-K237, which undergo large amplitude internal motions as reflected by small ^{15}N-^1H NOEs (<0.55). The description of motions in these conformationally labile residues usually required use of 3-parameter models, particularly the Clore model but also the LS model incorporating a chemical exchange contribution. Fits involving 3-parameter models returned goodness-of-fit statistics $\chi^2_i \approx 0$, so dynamic residues described by these models did not contribute to the cumulative sum of χ^2_i over all residues (χ^2_{tot}). Of the 44 residues included in the relaxation analysis, only 13-18 within the comparatively rigid

helical regions and their boundaries contributed to χ^2_{tot}. For these residues in regions of low or intermediate mobility the choice of model often varied with τ_M without a significant effect on χ^2_i. Such compensatory effects complicated selection of the global correlation time τ_M since fits within the range 6 ns $<\tau_M<$8.3 ns satisfied the global goodness-of-fit condition $\chi^2_{tot} <\chi^2_{crit}$ (n_{DF}) and returned reasonable χ^2_i and physically meaningful local motional parameters for all residues. Various empirical criteria were therefore examined during selection of τ_M. These include monitoring changes in the choice of motional model along the primary sequence (18), the value of τ_M predicted by a trimmed R_2/R_1 analysis for residues undergoing fast internal motions, and reconciliation with the larger radius estimated from the translational diffusion coefficient (see below). These criteria resulted in selection of a τ_M value of 7.7 ns, which also corresponds to a local minimum in χ^2_{tot}, for computation of the reported internal motional parameters.

An independent estimate of τ_M=8.3±0.5 ns was obtained from the translational diffusion coefficient using Equations 2 and 3. The derived τ_M lies near the upper bound of the range of values deemed consistent with the relaxation data. Discrepancies between the values of τ_M suggested by the two techniques may be due to model approximations inherent in the SE and SED equations, particularly the assumption of sphericity. For particles of equal volume, deviations from a spherical particle shape increase D (24) . This explanation is viable as the diffusion measurement sampled two different conformations corresponding to the cis and trans amide isomers of Pro232, while the relaxation measurement focused on resonances assigned to the trans isomer and was less affected by conformational exchange. However, this hypothesis requires that the aspect ratio of the SDS complex formed by the cis species be much larger ($\Delta p>>1$) than that of

the *trans* conformer. Since this condition is unlikely to have been fulfilled, we favor other explanations. For instance, an alternative possibility for the comparatively short τ_M obtained from relaxation measurements is motion of the protein fragment *within* the SDS aggregate, which would effectively decouple the measured translational and rotational diffusion rates. This explanation is plausible given that the protein occupies only ~16% of the volume in the complex assuming typical values of the protein specific volume.

The pattern of the order parameters S^2 along the primary sequence is generally mirrored by structural evidence from ^{13}C chemical shifts, ^{1}H -^{1}H NOEs, and $^{3}J_{\alpha N}$ (Fig. S1). Residues K218-M228 and K235-S247 exhibit high order parameters (S^2>0.75) as well as $^{3}J_{\alpha N}$ couplings, NOEs and chemical shifts consistent with persistent helical structure. A greater rigidity of helix 2 compared to helix 3 is revealed in both higher order parameters and by a more dense pattern of long range NOEs for helix 2. On the other hand, the low order parameters *and* extensive pattern of NOEs in helix 1 (G[-1]-K215) might be better explained as the result of concerted motions of the entire helix relative to the remainder of the molecule. The abrupt discontinuity in S^2 at residues S217-K218 marks the position of a flexible joint between helices 1 and 2, while a broader cleft including residues E229-I234 marks the break between helices 2 and 3. Persistently high order parameters (S^2>0.7) hint at structure up to residue M250. Beyond this point evidence of structure may be inferred from other NMR parameters as far as residue V261, but not as clearly from S^2, which decreases rapidly and smoothly in value above M250.

The order parameters S^2_{RCI} computed with MICS from chemical shifts (Fig. 7) are overall in good agreement with S^2 derived from relaxation data, particularly for helix 2.

In other segments of the sequence S^2_{RCI} tends to be larger than S^2. Since high S^2_{RCI} generally reflects low conformational flexibility, the difference in the two order parameters is possibly due to rapid relative reorientations of helical segments. This is consistent with a short segment such as helix 1 reorienting rapidly relative to the other segments. Such reorientations can preserve the secondary structure within the segments and would thus not alter chemical shifts. S^2 is also slightly reduced in helix 3 compared to helix 2. The greater flexibility of helix 3 is consistent with exchange between α-helical and a small population of 3_{10} structures within the broader basin of helical conformations, as suggested by the NMR structural ensemble.

pH Perturbation

The effect of an increase in the solvent pH from 6.0 to 7.0 on backbone amide $^1H^N$ and ^{15}N chemical shifts for SDS-bound $YscU_{CN}$ (Fig. S3) served as an additional probe of the extent of solvent exposure of different residues in the protein. While free Glu and Asp sidechains in water at RT have an intrinsic acid dissociation constant in the range 3.5-4.5, acidic or basic residues (Glu, Asp, Lys, Arg and His) within helical peptides and proteins complexed with SDS can undergo pKa increases of ~1-2 units when localized within the environment created by proximal sulfate headgroups at the solvent interface (25) (26). The increase in pK_a translates into an enhanced chemical shift response of nearby nuclei, such as backbone amide $^1H^N$ and ^{15}N, when the pH is in the range 6-7, and explains the pH sensitivity of ^1H-^{15}N HSQC chemical shifts for residues in the second helix (residues K218-S231) and in the vicinity of H242 (residues R238-F241) within the $YscU_{CN}$-SDS

complex. The chemical shift response is significantly lower in the first helix, in the linker region involving residue P232, and for residues >M250, indicating that these segments are positioned away from the micellar interface. The response is also attenuated in the third helix, with a prominent local maximum in the response at H242.

Amide Exchange Measurements

Fast $^{1}H^{N}$ exchange rates determined with the CLEANEX-PM experiment and derived protection factors P_{solv} permit identification of solvent-exposed regions of the backbone and exchangeable sidechain protons (Fig. S4). Two principal mechanisms slow exchange in the SDS complex: burial in the interior of the complex, which shields exchangeable protons from the solvent, and the formation of long-lived intramolecular hydrogen bonds associated with secondary structure. The small protection factor (P_{solv}=3.3) of the N-terminal residue L[-2] is consistent with absence of secondary structure and high solvent exposure. P_{solv} in subsequent residues G[-1] to K215 is ~10-100× larger indicating burial within the complex or participation in the first alpha helix. Most residues in the Glu-rich region between E220 and S231 corresponding to helix 2 display intermediate protection factors (≈10) although basic residues R223 and K226 have larger P_{solv} which appears consistent with an amphipathic helix with alternating protected and exposed regions. The segment following P232 is more shielded with high protection factors exhibited around highly hydrophobic F241 within helix 3. There is a notable increase in exposure at Q246 marking the end of the third helix. Subsequent residues from M250 to S258 display a pattern of alternating large and small P_{solv}. Some evidence of secondary structure in that region comes from positive $\Delta\delta\ ^{13}C^{\alpha}$ chemical

shifts, suggesting the regularity in exposure may be due to helical structure. Rapid exchange rates of the C-terminal tail residues V261-N263 are consistent with solvent exposure and the absence of secondary structure, in agreement with the low order parameters derived from relaxation data and absence of other structural evidence, as well as a low D5S PRE for V261. The high solvent exposure of V259-V261 is somewhat surprising given the hydrophobic character of valine. These residues lack persistent secondary structure but may occupy interfacial positions with sidechains immersed in the micelle and the backbone accessible to water. In agreement with this location, weak ^{1}H-^{1}H NOESY crosspeaks were observed between water and $^{1}H^{N}$ of S258-A262. In summary, despite gaps in the sequential CLEANEX data, the pattern of exchange rates and protection factors is consistent with a positioning of the second amphipathic helix at an exposed interfacial position, significant burial of the C-terminal regions following P232 and particularly of the third helix, with a drop in solvent protection at the end of the third helix, and particularly for the terminal residues (>V259).

SUPPLEMENTAL TABLES

Table S1. Number of NMR restraints by type and violation statistics for NMR and geometric restraints computed for the final ensemble of 20 $YscU_{CN}$ structures generated with XPLOR-NIH and PROCHECK. [1]Ensemble average of the root-mean-squared deviation of restraint violations computed by XPLOR-NIH. [2]Standard deviation of the RMSD of the restraint violations, computed over the ensemble. [3]Average number of violations per structure as evaluated with the violation thresholds indicated in parentheses. [4]Dihedral angle restraints derived from chemical shifts with TALOS+.

NMR derived restraints	Number of restraints
Total distances (NOE)	203
Intraresidual distances (i=j)	39
Sequential distances (|i-j|=1	119
Short range distances (1<|i-j|<=4	45
Long range distances (|i-j|>4	0
Dihedral angle restraints[4]	80
J-coupling constant restraints	17

Restraint violations	RMSD[1] (SD[2])	Avg number of violations[3]
Bonds (Å)	0.002 (0.000)	0.0 (# viol. > 0.05 Å)
Angles (deg)	0.371 (0.010)	0.0 (# viol. > 5°)
Improper (deg)	0.272 (0.016)	0.0 (# viol. > 5°)
VDW (Å)		0.0 (# viol. > 0.2 Å)
NOE (Å)	0.013 (0.006)	0.0 (# viol. > 0.5 Å)
Dihedral angles[4] (deg)	0.134 (0.090)	0.0 (# viol. > 5°)
J-coupling constant (Hz)	0.392 (0.062)	0.0 (# viol. > 1 Hz)

Table S2: Bacterial strains and plasmids used in this study

Strains, plasmids, or constructs	Description[a]	Reference
E. coli strains		
BL21	IPTG-inducible T7 RNA polymerase	(27)
Top 10	Commercial one-shot competent cells	Invitrogen
Y. pseudotuberculosis strains		
YPIII(pIB102)	wild-type, parental strain, Km^r	
YPIII(pIB75)	*ysc*U null strain, $Km^{r\ r}$	(28)
Plasmids		
pGEX-6P3	Commercial vector with N-term. GST-fusion Cb^r	GE Healthcare
pBADmycHis A	Commercial vector for L-ara induced expression Cb^r	Invitrogen
Constructs		
YscU	*yscU* full length in pBADmycHis A	This study
$YscU_{K212A}$	$yscU_{K212A}$ in pBADmycHis A	This study
$YscU_{E213A}$	$yscU_{E213A}$ in pBADmycHis A	This study
$YscU_{K215A}$	$yscU_{K215A}$ in pBADmycHis A	This study
$YscU_{K218A}$	$yscU_{K218A}$ in pBADmycHis A	This study
$YscU_{E220A}$	$yscU_{E220A}$ in pBADmycHis A	This study
$YscU_{K222A}$	$yscU_{K222A}$ in pBADmycHis A	This study
$YscU_{R223A}$	$yscU_{E224A}$ in pBADmycHis A	This study
$YscU_{E224A}$	$yscU_{E224A}$ in pBADmycHis A	This study
$YscU_{K226A}$	$yscU_{K226A}$ in pBADmycHis A	This study
$YscU_{K222A/K226A}$	$yscU_{K222A/K226A}$ in pBADmycHis A	This study
$YscU^6$	$yscU^6$ (K212A, K215A, K218A, K222A, R223A and K226A) in pBADmycHis A	This study
GST-$YscU_C$	$yscU_C$ in pGEX-6p-3	(29)
GST-$YscU_C^6$	$yscU_C^6$ in pGEX-6p-3	This study
GST-$YscU_{CNK218A}$	$yscU_{CNK218A}$ in pGEX-6p-3	This study
GST-$YscU_{CNE220A}$	$yscU_{CNE220A}$ in pGEX-6p-3	This study
GST-$YscU_{CNR223A}$	$yscU_{CNR223A}$ in pGEX-6p-3	This study
GST-$YscU_{CNK222A/K226A}$	$yscU_{CNK222A/K226A}$ in pGEX-6p-3	This study

[a] Km^r, kanamycin resistance, Cb^r, carbenicillin resistance

Table S3: Primers used in this study

Primer name	Primer sequence (5'- 3')	Restriction sites
Primers for sub-cloning		
fw_pGEX_yscU$_{CN}$	cgcggatccTactatcaatatattaaggaactta	*Bam*HI
rv_pGEX_yscU$_{CN}$	tccccccggggttaattagctaccaccactgatgag	*Sma*I
Primers for site-directed mutagenesis		
fw_pBAD_yscU$_{FL}$	catgccatggtgagcggagaaaagacagag	*Nco*I
rv_yscU$_{FL}$_K212A	gctcattttaagttccgcaatatattgatagtattcaaaggc	
fw_yscU$_{FL}$_K212A	gcctttgaatactatcaatatattgcggaacttaaaatgagc	
rv_pBAD_yscU$_{FL}$	cggaattcttataacatttcggaatgttgtttc	*Eco*RI
rv_yscU$_{FL}$_E213A	gctcattttaagtgccttaatatattgatagtattcaaaggc	
fw_yscU$_{FL}$_E213A	gcctttgaatactatcaatatattaaggcacttaaaatgagc	
rv_yscU$_{FL}$_K215A	gctcattgcaagttccttaatatattgatagtattcaaaggc	
fw_yscU$_{FL}$_K215A	gcctttgaatactatcaatatattaaggaacttgcaatgagc	
rv_yscU$_{FL}$_K218A	gatctcatccgcgctcattttaagttccttaatatattgatag	
fw_yscU$_{FL}$_K218A	ctatcaatatattaaggaacttaaaatgagcgcggatgagatc	
rv_yscU$_{FL}$_E220A	ccatttctttgtactcgcgtttgatcgcatccttgctcat	
fw_yscU$_{FL}$_E220A	atgagcaaggatgcgatcaaacgcgagtacaaagaaatgg	
rv_yscU$_{FL}$_K222A	accctccatttctttgtactcgcgtgcgatctcatccttgctc	
fw_yscU$_{FL}$_K222A	gagcaaggatgagatcgcacgcgagtacaaagaaatggagggt	
rv_yscU$_{FL}$_R223A	ctccatttctttgtactcggctttgatctcatccttgctcat	
fw_yscU$_{FL}$_R223A	atgagcaaggatgagatcaaagccgagtacaaagaaatggag	
rv_yscU$_{FL}$_E224A	gctaccctccatttctttgtacgcgcgtttgatctcatcc	
fw_yscU$_{FL}$_E224A	ggatgagatcaaacgcgcgtacaaagaaatggagggtagc	
rv_yscU$_{FL}$_K226A	ctgggctaccctccatttctgcgtactcgcgtttgatctc	
fw_yscU$_{FL}$_K226A	gagatcaaacgcgagtacgcagaaatggagggtagcccag	
rv_yscU$_{FL}$_K222A/K226A	ctgggctaccctccatttctgcgtactcgcgtgcgatctc	
fw_yscU$_{FL}$_K222A/K226A	gagatcgcacgcgagtacgcagaaatggagggtagcccag	

Table S4. Selected physical chemical properties of $YscU_{CN}$ and helices 1-3 at pH 6.0 and 7.0: computed net charge, Wimley-White hydrophobicities (7) and Eisenberg hydrophobic moment (8).

pH	helix	residues	charge	hydroph[1] (w/if)	hydroph[2] (w/o)	hmoment[3]
6.0	1	211-215	1.0	3.1	6.9	2.4
	2	218-229	-0.9	11.6	25.9	3.9
	3	234-246	3.8	6.7	14.0	2.1
	$YscU_{CN}$		5.9	33.2	67.4	
7.0	1	211-215	1.0	3.1	6.9	2.4
	2	218-229	-1.0	11.6	25.9	3.9
	3	234-246	3.2	5.9	11.8	2.2
	$YscU_{CN}$		5.2	32.4	65.1	

1. ΔG for transfer from water to POPC vesicle interface (Wimley-White w/if hydrophobicities) in kcal/mol.
2. ΔG for transfer from water to octanol (Wimley-White w/o hydrophobicities) in kcal/mol.
3. Eisenberg hydrophobic moment, computed with $\Delta G_{w/if}$, in kcal/mol.

SUPPLEMENTAL FIGURES

Figure S1. Overview of NMR and computed parameters for $YscU_{CN}$ in complex with SDS micelles, summarizing residue-specific dynamic and structural properties (refer to text for detailed descriptions of individual methods). Residue properties are aligned with the primary sequence, with residues color coded according to polarity, red:Glu,Asp; blue: Lys,Arg,His. S^2_{RCI}: order parameters predicted on the basis of chemical shifts using RCI (30). S^2: order parameters from relaxation data. Prot fact: solvent protection factors computed from amide ^1H exchange rates. Empty bars indicate protection factors too large to quantify accurately. Asterisks indicate protection factors not quantified due to spectral overlap. D5S/Mn^{2+} PRE: Induced paramagnetic relaxation enhancements. $\Delta\delta$ pH: mean chemical shift response to pH 6$\rightarrow$7 perturbation. $^3J_{HNHA}$: (H^N,H^α) ^3J-coupling; filled black circles: $^3J<6Hz$; gray circles: $6Hz<{}^3J<8Hz$; empty circles: $^3J>8Hz$. $d_{mn}(i,i+j)$: ^1H-^1H dipolar couplings; for d(i,i+1) bars at residue i are proportional to NOE magnitude. Sequential $d_{\alpha N}$ have been scaled by $\times 1/2$ relative to d_{NN} and $d_{\alpha N}$. Empty bars indicate visible NOEs not quantified due to spectral overlap. Asterisks indicate NOEs not observed due to overlapping crosspeaks. For d(i,i+2-4) horizontal lines link residues involved in NOEs. $\Delta\delta^{13}C^\alpha$: difference of $^{13}C^\alpha$ shift from standard random coil value. MICS: bars indicate α-helical regions predicted from chemical shifts with program MICS (31), with regions where $S^2_{RCI}>0.7$ indicated. PSI-PRED: bars indicate predicted α-helical regions.

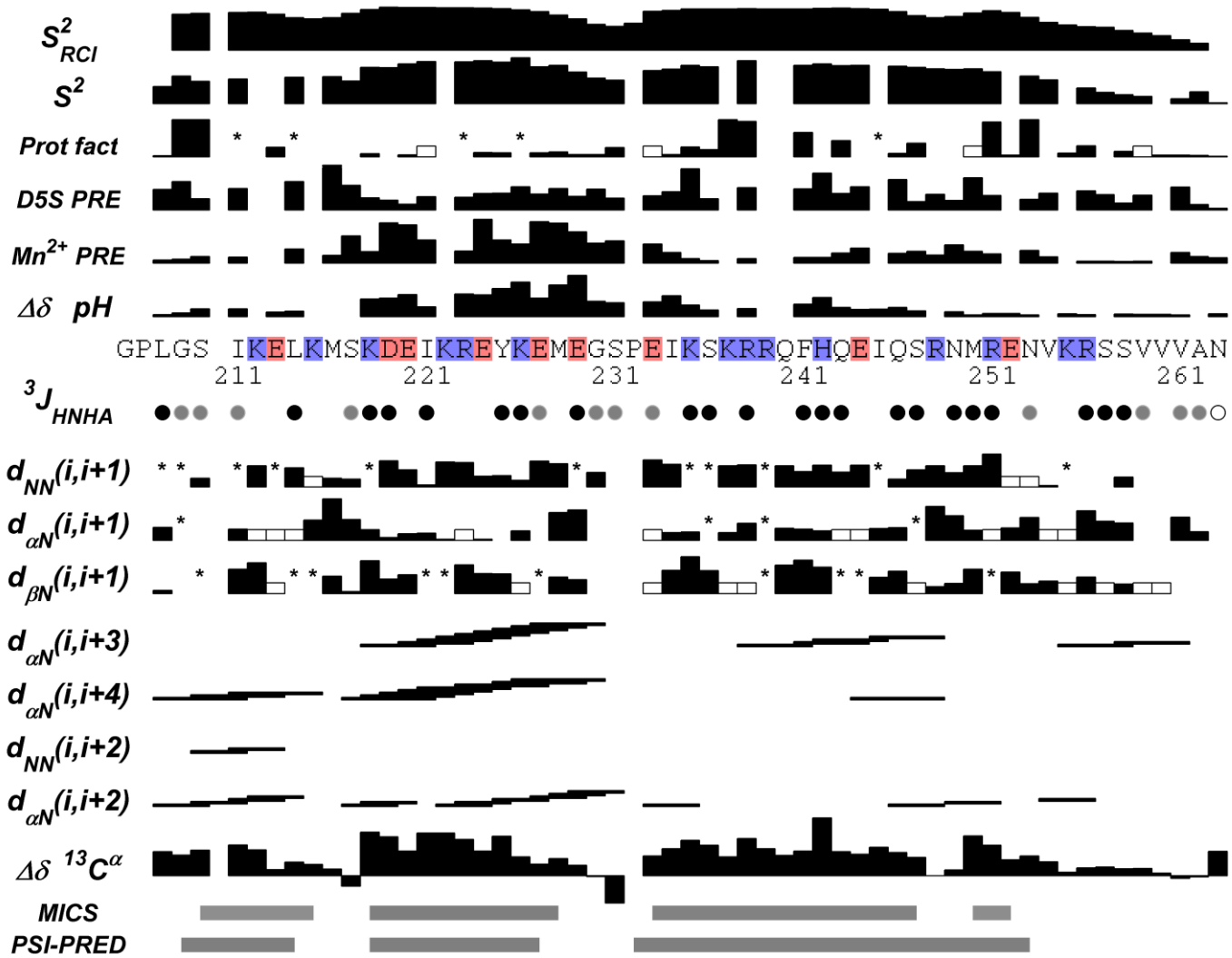
S^2_{RCI}
S^2
Prot fact
D5S PRE
Mn^{2+} PRE
$\Delta\delta$ pH
GPLGS IKELKMSKDEIKREYKEMEGSPEIKSKRRQFHQEIQSRNMRENVKRSSVVVAN
211
221
231
241
251
261
$^3J_{HNHA}$
$d_{NN}(i,i+1)$
$d_{\alpha N}(i,i+1)$
$d_{\beta N}(i,i+1)$
$d_{\alpha N}(i,i+3)$
$d_{\alpha N}(i,i+4)$
$d_{NN}(i,i+2)$
$d_{\alpha N}(i,i+2)$
$\Delta\delta\ ^{13}C^{\alpha}$
MICS
PSI-PRED

Figure S2. Relaxation data reveal global and residue-specific dynamics within the $YscU_{CN}$-SDS complex. Backbone ^{15}N NMR relaxation rates R_1 and R_2 and ^{15}N-^{1}H NOEs for $YscU_{CN}$ in complex with SDS, displayed against the primary sequence of $YscU_{CN}$.

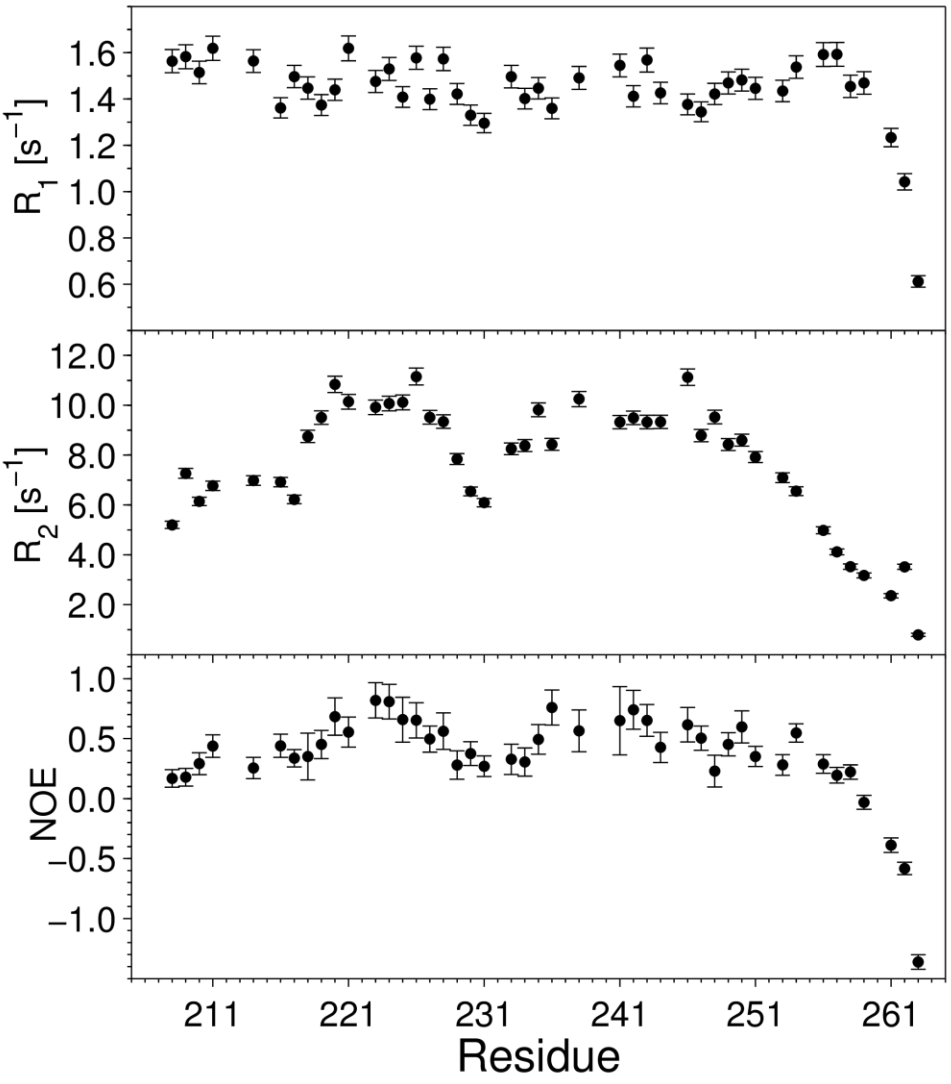

Figure S3. Residue specific chemical shift responses to a solvent pH perturbation correlate with local solvent exposure. Mean change in the backbone $^{1}H^{N}$, ^{15}N shifts in SDS-bound $YscU_{CN}$ due to an increase in pH from 6.0 to 7.0, displayed against the primary sequence of $YscU_{CN}$.

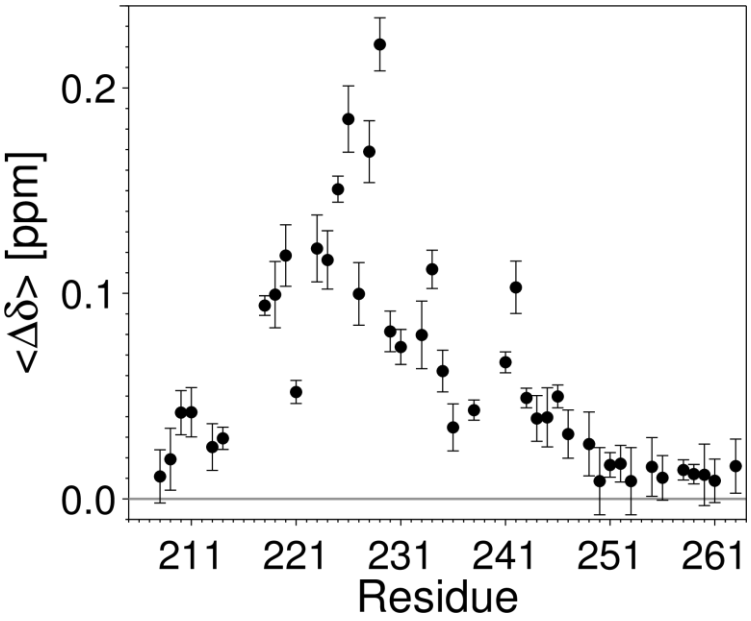

Figure S4. Solvent protection factors P_{solv} computed from backbone amide exchange rates for backbone amide H^N in SDS-bound $YscU_{CN}$, displayed against the primary sequence of $YscU_{CN}$. Small empty squares indicate residues exhibiting large but highly uncertain P_{solv} (k_{ex} below the detection limit).

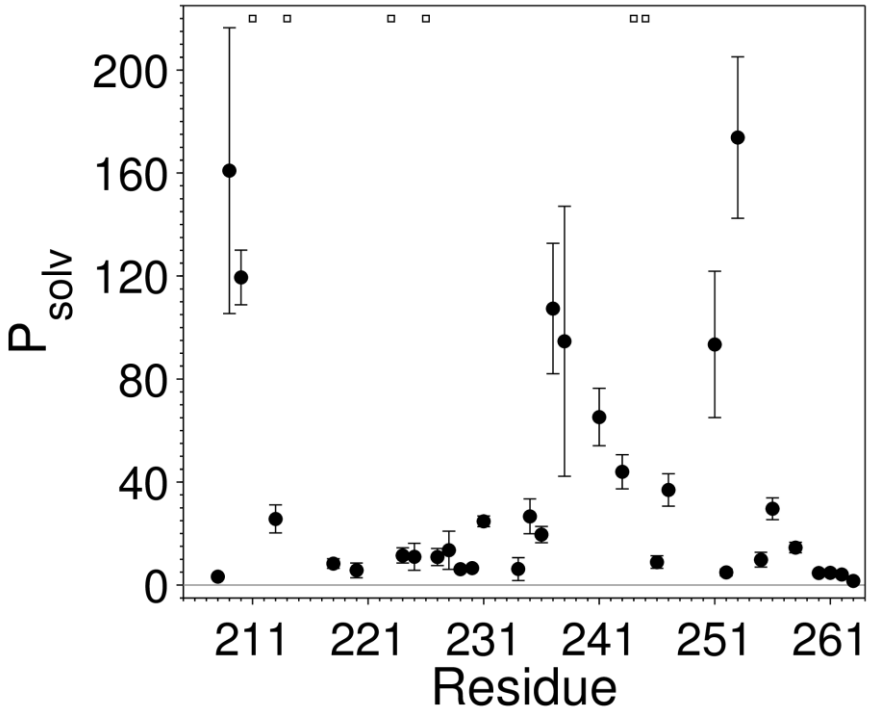

SUPPLEMENTAL REFERENCES

1. Schwieters, C. D., J. J. Kuszewski, and G. M. Clore. 2006. Using Xplor-NIH for NMR molecular structure determination. Prog Nucl Mag Res Sp 48:47-62.
2. Schwieters, C. D., J. J. Kuszewski, N. Tjandra, and G. M. Clore. 2003. The Xplor-NIH NMR molecular structure determination package. Journal of Magnetic Resonance 160:65-73.
3. Helgstrand, M., P. Kraulis, P. Allard, and T. Härd. 2000. Ansig for Windows: an interactive computer program for semiautomatic assignment of protein NMR spectra. J. Biomol. NMR 18:329-336.
4. Shen, Y., F. Delaglio, G. Cornilescu, and A. Bax. 2009. TALOS plus : a hybrid method for predicting protein backbone torsion angles from NMR chemical shifts. J Biomol NMR 44:213-223.

5. Laskowski, R. A., M. W. Macarthur, D. S. Moss, and J. M. Thornton. 1993. Procheck - a program to check the stereochemical quality of protein structures. Journal of Applied Crystallography 26:283-291.
6. Kabsch, W., and C. Sander. 1983. Dictionary of Protein Secondary Structure - Pattern-Recognition of Hydrogen-Bonded and Geometrical Features. Biopolymers 22:2577-2637.
7. White, S. H., and W. C. Wimley. 1998. Hydrophobic interactions of peptides with membrane interfaces. Biochim Biophys Acta 1376:339-352.
8. Eisenberg, D., R. M. Weiss, and T. C. Terwilliger. 1984. The Hydrophobic Moment Detects Periodicity in Protein Hydrophobicity. P Natl Acad Sci-Biol 81:140-144.
9. Kay, L. E., D. A. Torchia, and A. Bax. 1989. Backbone Dynamics of Proteins as Studied by N-15 Inverse Detected Heteronuclear Nmr-Spectroscopy - Application to Staphylococcal Nuclease. Biochemistry 28:8972-8979.
10. Hwang, T. L., P. C. van Zijl, and S. Mori. 1998. Accurate quantitation of water-amide proton exchange rates using the phase-modulated CLEAN chemical EXchange (CLEANEX-PM) approach with a Fast-HSQC (FHSQC) detection scheme. J Biomol NMR 11:221-226.
11. Mori, S., C. Abeygunawardana, M. O. Johnson, and P. C. van Zijl. 1995. Improved sensitivity of HSQC spectra of exchanging protons at short interscan delays using a new fast HSQC (FHSQC) detection scheme that avoids water saturation. J Magn Reson B 108:94-98.
12. Bai, Y., J. S. Milne, L. Mayne, and S. W. Englander. 1993. Primary structure effects on peptide group hydrogen exchange. Proteins: Struct. Funct. Genet. 17:75-86.
13. Connelly, G. P., Y. W. Bai, M. F. Jeng, and S. W. Englander. 1993. Isotope effects in peptide group hydrogen-exchange. Proteins: Struct. Funct. and Genet. 17:87-92.
14. Markley, J. L., A. Bax, Y. Arata, C. W. Hilbers, R. Kaptein, B. D. Sykes, P. E. Wright, and K. Wuthrich. 1998. Recommendations for the presentation of NMR structures of proteins and Nucleic Acids (Reprinted from Pure and Applied Chemistry, vol 70, pgs 117-142, 1998). J Mol Biol 280:933-952.
15. Buchan, D. W., S. M. Ward, A. E. Lobley, T. C. Nugent, K. Bryson, and D. T. Jones. 2010. Protein annotation and modelling servers at University College London. Nucleic Acids Res 38:W563-W568.
16. Jones, D. T. 1999. Protein secondary structure prediction based on position-specific scoring matrices. J Mol Biol 292:195-202.
17. Mandel, A. M., M. Akke, and A. G. Palmer. 1995. Backbone Dynamics of Escherichia-Coli Ribonuclease Hi - Correlations with Structure and Function in an Active Enzyme. J Mol Biol 246:144-163.
18. Fushman, D., S. Cahill, and D. Cowburn. 1997. The main-chain dynamics of the dynamin pleckstrin homology (PH) domain in solution: Analysis of N-15 relaxation with monomer/dimer equilibration. J Mol Biol 266:173-194.
19. Hall, J. B., and D. Fushman. 2003. Characterization of the overall and local dynamics of a protein with intermediate rotational anisotropy: Differentiating

between conformational exchange and anisotropic diffusion in the B3 domain of protein G. J Biomol NMR 27:261-275.
20. Wennerst.H. 1972. Nuclear Magnetic-Relaxation Induced by Chemical Exchange. Mol Phys 24:69-80.
21. Lipari, G., and A. Szabo. 1982. Model-Free Approach to the Interpretation of Nuclear Magnetic-Resonance Relaxation in Macromolecules .1. Theory and Range of Validity. J. Am. Chem. Soc. 104:4546-4559.
22. Lipari, G., and A. Szabo. 1982. Model-Free Approach to the Interpretation of Nuclear Magnetic-Resonance Relaxation in Macromolecules .2. Analysis of Experimental Results. J Am Chem Soc 104:4559-4570.
23. Clore, G. M., A. Szabo, A. Bax, L. E. Kay, P. C. Driscoll, and A. M. Gronenborn. 1990. Deviations from the Simple 2-Parameter Model-Free Approach to the Interpretation of N-15 Nuclear Magnetic-Relaxation of Proteins. J Am Chem Soc 112:4989-4991.
24. Ortega, A., and J. G. de la Torre. 2003. Hydrodynamic properties of rodlike and disklike particles in dilute solution. J Chem Phys 119:9914-9919.
25. Sheftic, S. R., R. L. Croke, J. R. LaRochelle, and A. T. Atexandrescu. 2009. Electrostatic Contributions to the Stabilities of Native Proteins and Amyloid Complexes. Methods in Enzymology, Vol 466: Biothermodynamics, Pt B 466:233-+.
26. Ma, K., E. L. Clancy, Y. B. Zhang, D. G. Ray, K. Wollenberg, and M. G. Zagorski. 1999. Residue-specific pK(a) measurements of the beta-peptide and mechanism of pH-induced amyloid formation. J Am Chem Soc 121:8698-8706.
27. Studier, F. W., and B. A. Moffatt. 1986. Use of Bacteriophage-T7 Rna-Polymerase to Direct Selective High-Level Expression of Cloned Genes. J. Mol. Biol. 189:113-130.
28. Lavander, M., L. Sundberg, P. J. Edqvist, S. A. Lloyd, H. Wolf-Watz, and A. Forsberg. 2002. Proteolytic cleavage of the FlhB homologue YscU of Yersinia pseudotuberculosis is essential for bacterial survival but not for type III secretion. J Bacteriol 184:4500-4509.
29. Frost, S., O. Ho, F. H. Login, C. F. Weise, H. Wolf-Watz, and M. Wolf-Watz. 2012. Autoproteolysis and intramolecular dissociation of Yersinia YscU precedes secretion of its C-terminal polypeptide YscU(CC). Plos One 7:e49349.
30. Berjanskii, M. V., and D. S. Wishart. 2007. The RCI server: rapid and accurate calculation of protein flexibility using chemical shifts. Nucleic Acids Res 35:W531-W537.
31. Shen, Y., and A. Bax. 2012. Identification of helix capping and b-turn motifs from NMR chemical shifts. J Biomol NMR 52:211-232.